NRC·CNRC

NRC Publications Archive
Archives des publications du CNRC

High entropy oxides as promising materials for thermal barrier topcoats: a review

Vakilifard, Hamideh; Shahbazi, Hossein; Liberati, Andre C.; Saraswathy, Rakesh B. Nair; Lima, Rogerio S.; Pugh, Martin D.; Moreau, Christian

This publication could be one of several versions: author's original, accepted manuscript or the publisher's version. / La version de cette publication peut être l'une des suivantes : la version prépublication de l'auteur, la version acceptée du manuscrit ou la version de l'éditeur.
For the publisher's version, please access the DOI link below./ Pour consulter la version de l'éditeur, utilisez le lien DOI ci-dessous.

Publisher's version / Version de l'éditeur:
https://doi.org/10.1007/s11666-024-01744-0
Journal of Thermal Spray Technology, 2024-03-04

NRC Publications Archive Record / Notice des Archives des publications du CNRC :
https://nrc-publications.canada.ca/eng/view/object/?id=fa126c6d-7df8-49e2-b2f8-37acfbd8ac32
https://publications-cnrc.canada.ca/fra/voir/objet/?id=fa126c6d-7df8-49e2-b2f8-37acfbd8ac32

Access and use of this website and the material on it are subject to the Terms and Conditions set forth at
https://nrc-publications.canada.ca/eng/copyright
READ THESE TERMS AND CONDITIONS CAREFULLY BEFORE USING THIS WEBSITE.

L'accès à ce site Web et l'utilisation de son contenu sont assujettis aux conditions présentées dans le site
https://publications-cnrc.canada.ca/fra/droits
LISEZ CES CONDITIONS ATTENTIVEMENT AVANT D'UTILISER CE SITE WEB.

Questions? Contact the NRC Publications Archive team at PublicationsArchive-ArchivesPublications@nrc-cnrc.gc.ca. If you wish to email the authors directly, please see the first page of the publication for their contact information.

Vous avez des questions? Nous pouvons vous aider. Pour communiquer directement avec un auteur, consultez la première page de la revue dans laquelle son article a été publié afin de trouver ses coordonnées. Si vous n'arrivez pas à les repérer, communiquez avec nous à PublicationsArchive-ArchivesPublications@nrc-cnrc.gc.ca.

National Research Council Canada | Conseil national de recherches Canada

Canada

High Entropy Oxides as Promising Materials for Thermal Barrier Topcoats: A Review

Hamideh Vakilifard[1*], Hossein Shahbazi[1], Andre C. Liberati[1], Rakesh B. Nair Saraswathy[1], Rogerio S. Lima[2], Martin D. Pugh[1], Christian Moreau*[1]

[1]Department of Mechanical, Industrial and Aerospace Engineering, Concordia University, Montreal, QC H3G 1M8, Canada.

[2]National Research Council of Canada, 75 de Mortagne Blvd, Boucherville, QC J4B 6Y4, Canada.

Corresponding authors: hamideh.vakilifard@mail.concordia.ca
Christian.moreau@concordia.ca

Abstract

Multi-layered thermal barrier coatings (TBCs) are deposited on gas-turbine metallic components to protect them against high temperatures, oxidation, and corrosion. However, TBCs have limited working temperatures and lifetimes due to their material properties. Several approaches are being tested to increase TBC topcoats' phase stability and properties. Increasing entropy to stabilize phases is a concept introduced in 2004 and required decreasing the Gibbs free energy. Many high-entropy ceramics are being developed for structural and functional applications, and different types of high-entropy oxides (HEOs) are promising TBC ceramics due to their unique characteristics. HEOs are single-phase solid solutions that contain five or more cations, usually a mixture of transition metals and rare earth elements. Due to the cocktail effect, the final material has a different behavior from its constituents, making it a viable method to improve the properties of traditional materials. Generally, high entropy materials are characterized by three additional phenomena: sluggish diffusion, severe lattice distortion, and high entropy. A review of possible improvements in the lifetime of TBC topcoats using different HEOs in terms of their composition, properties, and stability is presented here. Different HEOs are then examined and various thermophysical properties, high-temperature stability, and sintering resistance are discussed.

Keywords: High Entropy Oxides, Thermal Barrier Coatings, Topcoat, Thermal Spray.

Introduction

The Olympic motto “citius, altius, fortius – communiter” which means “faster, higher, stronger – together” tempts participants to work harder for new records. Likewise, the industrial sector has high-performance standards and pursues continuous improvement which is paramount to increasing sustainability in both aviation and industrial gas turbines (GT). Advancements in power generation, pollution reduction, and resource conservation are the driving forces behind the development of cutting-edge protective coatings. Within the domain of gas turbines (GTs), hot section components, such as combustors, turbine blades, and vanes, are covered with thermal barrier coatings (TBCs) to protect them against high temperatures and extend their lifespan (Ref 1–4). Driving hotter GTs is the major driving force in improving TBCs, which results in higher turbine efficiency, lower fuel consumption, and reduced NOx emissions (Ref 5–7).

TBC coatings are usually applied using thermal spray (TS) methods and comprise a metallic bond coat and ceramic topcoat, with a total thickness ranging from 200-1000 µm (Ref 8). TS processes may provide a variety of coating thicknesses that depend on the operating conditions of the components, for example, thinner coatings (e.g., 150-250 µm) on vanes prevent gas path reduction in GTs during operation, thereby preserving efficiency. In contrast, thicker coatings (e.g., 250-1000 µm) provide increased thermal insulation for hotter parts, such as combustors (Ref 9,10).

In TBC systems, a thermally grown oxide (TGO) layer forms at the topcoat and bond coat interface as aluminum diffuses out of the bond coat and oxidizes in contact with oxygen diffusing through the topcoat. This process ultimately leads to the depletion of the aluminum in the bond coat, creating a uniform alumina layer. While the bond coat protects the substrate against oxidation and corrosion, the topcoat - usually Yttria Stabilized Zirconia (YSZ) - insulates the underlying layers (Ref 2,4,11). Nevertheless, due to phase transformation, thermal shock, sintering, etc., YSZ has

limitations in terms of its maximum working temperature (e.g., 1200-1300℃) and exposure time (Ref 11–13). In this context, new ceramics with high phase stability and low thermal conductivity are being developed namely defect-cluster TBCs, rare earth zirconates (REZ) such as $Gd_2Zr_2O_7$, and high entropy oxides (HEOs). These next-generation materials are designed to address typical TBC challenges, such as thermal insulation, erosion, and Calcium Magnesium Alumina Silicate (CMAS) hot corrosion resistance (Ref 14–17).

The concept of increasing the entropy of ceramics to stabilize them at high temperatures (higher than 1200℃) was introduced recently by Rost *et al.* (Ref 18). As the newest candidates for ceramic topcoats, HEOs are composed of transition metal oxides and rare earth oxides (REOs). High entropy zirconates (HEZ), a subcategory of HEOs, are considered promising TBC topcoats. A review of the literature suggests that compared to YSZ, HEZ exhibits lower thermal conductivity and high phase stability, coupled with a high coefficient of thermal expansion (CTE). The properties will result in an improved performance at higher temperatures (higher than 1300˚C) and match the characteristics of their underlying layers, including both the bond coat and the substrate. In addition, HEZs demonstrate superior sintering resistance (Ref 19–23) and the potential to reduce residual stresses in the coating. By using coatings that are designed to withstand higher thermal and mechanical stress levels, while being highly insulating, and ensuring compatibility with metallic components in terms of thermal expansion, it becomes possible to extend the lifetime of the TBC and the interval between GT maintenance (Ref 24). These promising features of HEOs make them an ideal candidate for topcoats, warranting further investigation. Hence, this review delves into novel ceramic topcoats, particularly HEOs focusing on their thermo-physical properties, and their potential to enhance TBC performance.

Lastly, it is essential to note that although the impact of powder manufacturing methods on HEO properties has been recognized as significant, it remains an aspect not been investigated in our study. Our current research does not focus on exploring the specific aspect of how different manufacturing methods may influence HEO properties. Instead, we aim to thoroughly investigate and analyze the properties of HEOs to gain valuable insights into their performance, characteristics, and potential applications. Focusing on these aspects allows us to contribute to existing knowledge in this field. Additionally, we hope to pave the way for future research in the field of HEOs.

Current TBC Topcoat Ceramics

In TBC systems an overlay ceramic topcoat is deposited on a bond coat to reduce the heat flux toward the bond coat and substrate, therefore safeguarding them against high temperatures (Ref 8). The TGO layer plays a crucial role in TBC systems. Its main function is to act as a diffusion barrier, preventing the migration of harmful species such as oxygen and sulfur from the working environment to the underlying bond coat and substrate. Ultimately it helps to maintain the integrity and durability of the TBC system by reducing the detrimental effects of oxidation and corrosion. Additionally, the TGO layer provides thermal insulation, contributing to the overall thermal resistance of the TBC system and enabling effective thermal management in high-temperature applications.

While the bond coat protects the substrate against oxidation and corrosion, the topcoat (usually yttria-stabilized zirconia, ZrO_2-6-8wt%Y_2O_3, or YSZ), insulates the underlying layers (Ref 2). A functional TBC topcoat must withstand high-temperature environments without undergoing phase

transformation, making phase stability one of the most critical requirements for topcoats (Ref 10,25). In addition, low thermal conductivity, high CTE, as well as good fracture toughness are essential (Ref 12,25,26). YSZ has been found to be a good material to meet these criteria, with excellent properties to tolerate the harsh environment of GTs:

- Low thermal conductivity compared to Ni-based superalloys (2.6 W/mK for the bulk 5.3 wt.% YSZ, at 600 °C and 0.7 to 1.4 W/mK for 7.25 wt.% YSZ coating (Ref 11), while the thermal conductivity value is between 16-23 W/mK for Ni-based superalloys at 600 °C, depending on the chemical compositions (Ref 27)).
- High coefficient of thermal expansion (CTE): (11×10^{-6} 1/K (Ref. 11)), which is very close to those of bond coat materials and Ni-based substrates ($13\text{-}15 \times 10^{-6}$ 1/K (Ref 27)).
- High fracture toughness value compared to other ceramics such as toughened Si_3N_4, and Al_2O_3 (Ref 28), (2 $MPa.m^{1/2}$ (Ref 1)).

YSZ is practically a thermal insulator, with the phonon scattering properties of its atomic lattice reducing the heat flux toward the underlying layers. Phonon scattering occurs mainly by point defects such as oxygen vacancies and substitutional solid atoms. Moreover, line defects such as dislocations, or grain boundaries can also result in phonon scattering (Ref 29,30). In addition, the high CTE of YSZ allows it to relieve stresses due to the CTE mismatch between the YSZ and metallic layers (Ref 31). High-temperature mechanical properties, such as fracture toughness, hardness, and elastic modulus play a pivotal role in the failure of the coatings due to crack propagation erosion, and foreign object damage (FOD) (Ref 3,11,32). Nevertheless, after operation mechanical and microstructural properties of materials through processes like densification, microcrack healing, or stress relaxation will change. Such changes could be

beneficial for the GT components operating at high temperatures for extended periods of time (Ref 33–35).

Meanwhile, there are several factors that contribute to the limited lifespan of TBCs. First stresses arise from thermal expansion mismatch between ceramics and metals. Also, the oxidation of metals and the growth of TGO changes the microstructure of the coating due to sintering and changing the coating properties (Ref 36). Besides, ensuring the chemical compatibility of the ceramic topcoat with both the TGO layer and metallic bond coat enhances adhesion between layers, subsequently improving the lifetime and durability (Ref 12). In addition, corrosion (usually caused by molten silicate deposits or CMAS derived from sand deposits or volcanic ash) deteriorates the coating by diffusing through the pores and defects. Molten CMAS infiltrates, and reacts with the ceramic, forming a dense glassy reaction zone, which eventually accelerates the sintering (Ref 8,37). The presence of these reaction zones intensifies elastic strain levels in the coatings. High elastic energy release rates in the presence of glassy reaction products may compromise the strain tolerance of TBCs. The delamination cracks inside or beneath the infiltrated layer typically originate from surface-connected vertical cracks occurring as a result of processing defects or during service due to sintering or cold shock and eventual spallation of the coatings (Ref 38–40). Ultimately, the failure is thermomechanical, arising from the strain energy generated in the coatings while cooling due to the CTE mismatch between the CMAS-infiltrated topcoat and the underlying layer (Ref 41).

Microstructural changes (Ref 31) can also cause stresses at the topcoat/bond coat interface and within the topcoat (Ref 42). Furthermore, during the thermal spraying of YSZ, a metastable phase (t') is developed by activating a ferroelastic toughening mechanism and providing sufficient toughness to withstand the harsh GT environment. But the eventual phase

transformation at 1200℃ after long times from t' to the tetragonal and cubic structures are followed at high temperatures accompanied by volume expansion, which finally decreases the toughness (Ref 8,11,13). The transition from t' to the cubic phase results in a significant volume increase, impacting stress distribution in the coating TBCs and exacerbating thermomechanical failure (Ref 43). Additionally, the t' to cubic transformation can lead to the formation of vertical cracks at high temperatures, as the cubic phase exhibits less toughness than the t' phase (Ref 28). Another harmful transformation during cooling or heating happens, when the tetragonal phase transforms into a monoclinic phase, leading to 5-7% volume changes (Ref 44) and promoting microcrack nucleation. Hence, YSZ has a maximum operating temperature of about 1200°C (Ref 45).

TBC lifespan is also limited due to spallation and/or delamination within the topcoat interface with TGO, where crack nucleation and propagation may occur due to tensile stresses resulting from the outward growth of the TGO (Ref 46). During TBC operation, sintering typically occurs due to prolonged exposure to high temperatures, reducing pores size and percentage (Ref 4,36). This rapid increase in thermal conductivity causes stress at the topcoat and bond coat interface and within the topcoat (Ref 42,47). On the other hand, although stress relaxation mechanisms are expected to occur at high temperatures, sintering also tends to induce residual stresses within the coating after long-time operations.. During the sintering process, in-plane shrinkage takes place, accompanied by an in-plane elastic strain. In-plane shrinkage is also present due to thermal expansion mismatch between the topcoat and underlying layers at their operational temperatures. Once the in-plane tensile stresses exceed the fracture energy of the topcoat, the coating may fail through spallation (Ref 48,49).

In this regard, new ceramics are developed to address the usual TBC issues including the defect cluster TBCs, rare earth zirconates (REZ) such as $Gd_2Zr_2O_7$, and high entropy oxides (HEO) (Ref 14). The novel materials are designed to address the usual TBC challenges faced by TBCs, such as thermal insulation, CMAS hot corrosion resistance, sintering resistance, and compatibility with TGO and bond coat (Ref 14–17).

Novel Topcoat Ceramics

To enhance TBC topcoats, different ceramics have been studied and introduced as promising candidates. Initially, topcoat ceramics are selected based on criteria such as low thermal conductivity, high CTE, and excellent phase stability. Subsequently, additional factors like toughness, hardness, thermal cycling behavior, and hot corrosion resistance must be thoroughly investigated. Diverse ceramics including REOs or defect cluster TBCs, rare-earth zirconate (REZ), Perovskites, Hexa-aluminates, and Phosphates, have been explored (Ref 1,8,11). Vassen *et al.*(Ref 8) have compiled a substantial amount of data concerning the thermal conductivities and CTEs of various materials (Figure 1). The properties are of great interest when comparing them to conventional YSZ. In line with previous discussions, ceramics with low thermal conductivity and high coefficient of thermal expansion (CTE) values are considered highly desirable. In this vein, ceramics such as REZ with the composition of $RE_2Zr_2O_7$ (in which RE can represent any rare-earth element), multi-component zirconia-based ceramics, and high entropy oxide (HEO) consisting of at least five different cationic elements with 5-35 atomic% in their composition with high mixing entropy, exhibit the desired properties. This review article provides an explicit focus on HEOs.

REZ materials with pyrochlore or defective fluorite structures are among the most extensively studied for TBC applications, particularly CMAS attack, as well as high-temperature environments exceeding 1300℃ (Ref 14).

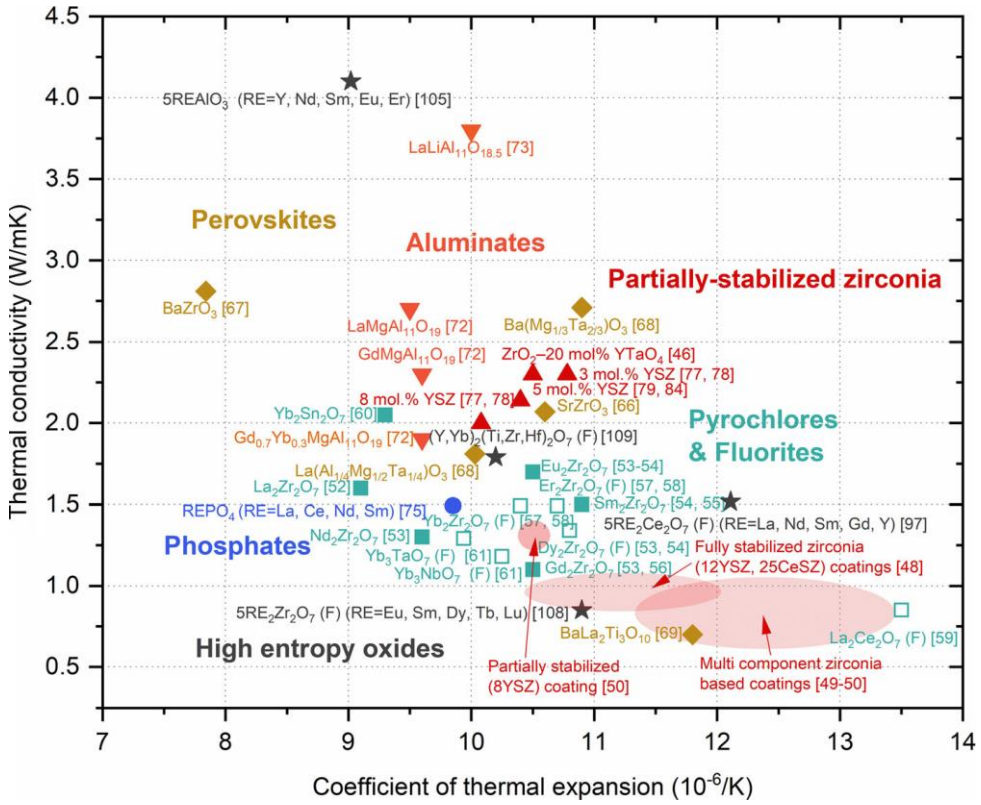

Figure 1: CTE vs. thermal conductivity of different TBC topcoat materials gathered by Vassen *et al.* (Ref 8).

Ceramics featuring a pyrochlore crystal structure typically adopt either an $A_2B_2O_7$ or $A_2B_2O_6O'$ configuration. Here, A and B represent cations of rare-earth elements and transition metals with charge states 2+, 3+, 4+, and 5+, forming a face-centered cubic (FCC) array. The stability of A and B cations in pyrochlores can be achieved by maintaining the ionic radius ratio of A and B ($^{r_A}/_{r_B}$) within the range of 1.46 and 1.80 (Ref 50). For instance, the ratio for different lanthanide zirconates (Ln can be La, Nd, Sm, Eu, or Gd), varies between 1.46 and 1.61, leading to the formation of a

pyrochlore structure. Conversely, for ratios below 1.46, a defective fluorite structure will be more stable (Ref 51). A comparison of cations' positions certifies that the pyrochlore has a higher degree of order than that of the defective fluorite structure. One challenge with the pyrochlore structure is an order-disorder transformation, a characteristic shared by all lanthanide zirconates, which is likely dependent on the lanthanide ion radius. The transition temperature for Gd is reported to be 1550-1570℃ (Ref 52) and 2000℃ for Sm. In contrast, La did not undergo this transformation (Ref 14). The transformation is reported to affect the sintering rate of coatings (Ref 11,47).

Lanthanide zirconates exhibit low thermal conductivity owing to their high oxygen vacancies and large atomic mass differences between Ln and Zr, leading to increased phonon scattering. Thus, they are potential topcoat candidates (Ref 11,53,54). Additionally, compared to YSZ good CMAS corrosion resistance (Ref 55) and higher temperature stability further explain the reason for their potential. Recently $La_2Zr_2O_7$ (Ref 56,57), $Nd_2Zr_2O_7$ (Ref 58,59), $Gd_2Zr_2O_7$ (Ref 60), and $Sm_2Zr_2O_7$ (Ref 61,62) have been introduced as alternatives for TBC topcoats (Ref 63–65). Among them, $Gd_2Zr_2O_7$ stands out with its exceptional thermophysical properties, with lower thermal conductivity (1.2-1.4 W/mK for bulk ceramic), higher CTE (10.5-12.2 $\times 10^{-6}$ 1/K), as well as superior thermal stability (1550℃), compared to YSZ, which made it an interesting alternative for the topcoat (Ref 11,66). However, the mechanical properties of $Gd_2Zr_2O_7$, such as elastic modulus and fracture toughness need to be improved in order to increase erosion resistance and FOD. Further improvements in the thermal resistance of the TBC can be attained by implementing microstructural modifications. These modifications include augmenting the overall thickness of the TBC and/or decreasing its thermal conductivity by increasing porosity or utilizing new TBC materials characterized by lower thermal conductivity values compared to YSZ (Ref 67). Nevertheless, it is worth noting that the introduction of new REZs led to compromised topcoat

performance during thermal cyclic tests (Ref 66), and low damage resistance attributed to their low fracture toughness values (less than half of YSZ (Ref 68) and lower CTE values (Ref 57,64). The thermochemical incompatibility of REZ with the TGO layer is an issue, impacting the lifetime of the coating (Ref 69,70). These shortcomings necessitate using REZ together with a YSZ topcoat to form a double-layered ceramic (DLC) coating (Ref 57,71). Therefore, upgrading materials to pyrochlores may be more effective by applying other modifications, such as using DLC topcoats for high temperatures, as Vassen *et al.* (Ref 72) claimed, or using graded topcoats for moderate temperature applications, according to Chen *et al.* (Ref 73).

High Entropy Materials

The concept of high entropy alloys was introduced first and later extended to ceramics. High entropy alloys are simple solid solutions containing five or more elements with 5-35 atomic percent, in equiatomic or non-equiatomic ratios (Ref 74). Yeh *et al.* (Ref 75) presented four distinct effects for high entropy alloys (HEAs), that could be extended to high entropy ceramics. Thermodynamically, HEAs have high configurational entropy ($\Delta S > 1.61R, R$ is the gas constant: 8.314 J/K mol). The high entropy effect could interfere with the formation of complex phases in thermodynamics. Besides, HEAs have severe lattice distortion that can change the properties of the final composition from the primary constituents. Furthermore, in terms of kinetics, HEAs have severe sluggish diffusion that limits phase transformation. Lastly is the cocktail effect, which is the ability of materials to develop a wide range of unique and unexpected properties by combining them. The new properties depend on a few parameters including the mixture rule, mutual interactions between all the elements, and severe lattice distortions due to mass and bonding

differences. Among the aforementioned core effects, the high configurational entropy plays a vital role in enhancing high-temperature stability (Ref 76). A comprehensive assessment of performance, perspectives, and future applications of thermally sprayed HEAs has been conducted by Nair *et al.* (Ref 77) and Shahbazi *et al.* (Ref 78).

Crystal Structures of HEOs

HEOs, which belong to the category of high entropy ceramics (HECs), are characterized as solid solutions consisting of five or more principal elements, with equal or non-equal compositions (Ref 76). Some reviews have been published for bulk HECs and are still underway (Ref 20,21,79–81). In this section, a subset of HEOs will be studied specifically for TBC topcoats. HEOs can generally be stabilized in different crystal structures such as rock salt (Ref 18,82), fluorite (Ref 83–86), perovskite (Ref 87,88), pyrochlore (Ref 89–93), bixbyite, magneto plumbite (Ref 94), O^{3-} type layered (Ref 95), or spinel (Ref 96–98). According to the studies, all types of oxide crystal structures, or different phases can be effectively designed with an entropy-based approach, by selecting the cations according to their ionic radii and oxidation state (Ref 81,99). In addition, the presence of different cations produces various structures or phase compositions (Ref 100). The pyrochlore oxide's complex structure exhibits strong phonon scattering characteristics. Over the past few years, various types of high-entropy oxides with pyrochlore structures have been investigated (Ref 22,83,92,100).

Stabilizing HEOs

Multi-component or entropy-stabilized oxides (ESO) were first introduced in 2015 by Rost *et al.* (Ref 18), by fabricating a stable single-phase oxide using five equimolar oxides including MgO, CoO, NiO, CuO, and ZnO. The selection of these oxides was based on factors such as electronegativity values, crystal structures, cation coordination, and solubility binary oxides. The concept was first having a stable composition at high temperatures without any transformations. In this research, a group of five oxides with an equimolar ratio was studied, and the relationship between mixing entropy (configurational entropy) and the composition of a mixture was calculated. Based on their findings, it was established that deliberate configurational disorder provides a strategy for discovering new phases. In addition, it provides unexplored opportunities for property engineering. Chen *et al.* (Ref 19) synthesized a five-component ESO with a composition of $(Ce_{0.2}Zr_{0.2}Hf_{0.2}Sn_{0.2}Ti_{0.2})O_2$, with a low thermal conductivity (1.2 W/mK), suggesting the composition as a promising ceramic for TBCs based on the thermophysical properties.

The phase stability, according to Gibbs free energy, not only depends on the ideal configurational entropy but also on the temperature and mixing enthalpy. The following equation (Equation 1) gives the Gibbs Free energy in an ideal solid solution. Nevertheless, contributions from configuration, vibration, electronic excitation, and magnetism affect the free energy amount (Ref 101). More accurate free energy calculations for high entropy ceramics are done by different teams and can be found in (Ref 102–108).

$$\Delta G_{mix} = \Delta H_{mix} - T\Delta S_{mix} \qquad \textbf{(1)}$$

In which ΔH_{mix} is the mixing enthalpy, $\Delta S_{mix}$is the mixing entropy, and T is the absolute temperature. In the aforementioned papers, enthalpy and temperature have to be increased in order to achieve high entropy values, meaning that the enthalpy value always must be positive (+ΔH). In this equation, the temperature parameter also becomes very significant. This means that the single phase will be stable at higher temperatures, and at lower temperatures, it transforms into a multi-phase structure (Ref 22).

Configurational entropy, in particular, has a considerable effect on the high entropy materials. As highlighted by Ananad *et al.* (Ref 102) configurational entropy becomes more critical as the number of cations in multi-component oxides increases, affecting stability in single phase solid solutions. In addition, to predict the formation of a single-phase HEO, an indicator has been introduced based on atomic size differences (δ) of A-site and B-site cations, as well as the enthalpy of mixing (ΔH_{mix}) (Ref 22,109–112). Equation 2 gives the descriptor based on atomic size differences:

$$\delta = \sqrt{\sum_{i=1}^{N} c_i \left(1 - \frac{r_i}{\sum_{i=1}^{N} c_i r_i}\right)^2} \qquad \textbf{(2)}$$

In which c_i is the concentration of species and r_i is their radius. Huttere *et al*. (Ref 113) reported a threshold of 4.5% for δ to form a single-phase Zirconate, while Yang *et al.* presented a 5.2% threshold (Ref 109), which seems to be very close to each other.

On the other hand, Wen *et al.* (Ref 104) introduced a descriptor based on both mixing enthalpy and atomic size differences, using the logistic regression approach in supervised machine learning. This descriptor was first introduced for borides with the composition of $(M_xN_{1-x})B_2$. Furthermore,

Sarker *et al.* (Ref 114) introduced an entropy formation ability descriptor based on mixing enthalpy, based on the energy spectrum of the high entropy system at absolute zero. Still, it seems that all introduced descriptors are in their early stages or are just applicable to specific systems.

Nevertheless, they provide a convenient means to facilitate the discovery and design process for high entropy ceramics. Spiridigliozzi *et al.* (Ref 85) also studied a predictor for single-phase HEO formation, emphasizing the "dispersion" of cationic radii as a key parameter, rather than the cationic mean radius. In parallel, a descriptor by density functional theory (DFT) method was developed by Pitike *et al.* (Ref 115). This method considers oxygen vacancy concentrations and local distortions to predict the single-phase formation of pyrochlore HEO. However, exploring new HEOs may be facilitated if a simple indicator were used. Given their compositional diversity, there are several structural and chemical combinations that may be achieved. As a result, attempting to find the "optimal properties" experimentally for specific applications can be time-consuming and frustrating. According to theoretical approaches such as density functional theory (DFT) calculations, it appears to be possible to calculate phase equilibria, structures, and (some) properties of HEOs. For systems with such complexity, traditional simulation approaches might still be challenging though (Ref 116–118). The discovery of novel HEOs with specific properties can thus be accelerated using combinatorial synthesis and high-throughput calculations. There is no doubt that HEOs will progress more rapidly if experimental and theoretical researchers collaborate more actively.

Properties of HEOs

In recent years, functional properties of HEOs have been the subject of extensive research, covering various aspects such as mechanical (Ref 118,119), thermal (Ref 86,120), dielectric (Ref 121), electrochemical (Ref 122), optical (Ref 123), and magnetic (Ref 124,125) properties. Due to their high-entropy nature, HEOs have notably different properties from their individual constituents. These properties can be tailored appropriately to suit specific materials applications by selecting primary constituents and calculating thermodynamics. In the literature, ESO and HEO terms are used interchangeably. As discussed by Chen *et al.*(Ref 19), Liu *et al.* (Ref 22), and the preceding section, the degree of entropy in HEOs is essentially determined by their mixing entropy. On the other hand, ESOs have high mixing entropy, as well as positive enthalpy and entropy, dominating thermodynamic stability. In other words, enthalpy also affects phase formation and stability. However, the long-term performance or the effects of volume-changing transformations require more investigation. In addition, ESOs, undergo a reversible transformation at a specific transition temperature, transitioning from a multi-phase composition to a single-phase composition. Since not all aspects of multiphase ceramics' long-term performance are fully understood, and phase transformations might be accompanied by unexpected volume changes, single phase compositions are typically preferred. This preference is one of the main reasons for favoring HEOs over ESOs.

According to the literature, HEOs have lower thermal conductivity compared to oxide ceramics (Ref 93,126) due to phonon scattering, resulting from the severe lattice distortion effect of high entropy and their slow sluggish grain growth rate. Similar behavior has also been observed in HEAs (Ref 127).

Furthermore, thanks to the sluggish diffusion effect of high entropy materials, the sintering rates tend to be relatively lower compared to conventional materials. This characteristic contributes to enhanced coating performance during thermal cycling and contributes to decreased thermal conductivity values (Ref 128,129). Other main properties reported in the literature, that are essential for TBC candidates such as CTE, phase stability, and fracture toughness have been summarized in Table 1. In this table, the properties of benchmark bulk YSZ are provided in the first line for comparison with other HEOs. P or F in the table represents pyrochlore and fluorite. Notably, the table illustrates that new HEOs exhibit desirable properties, including low thermal conductivity and high thermal stability. However, it's important to highlight that only a few researchers have investigated other crucial properties that significantly impact the lifetime and performance of TBCs in GTs, such as fracture toughness and hardness, which are important for crack propagation and FOD.

Potential High Entropy Oxides for TBCs

To date, several HEOs have been designed, synthesized, and studied for TBC purposes. These novel ceramics primarily exhibit pyrochlore or fluorite structures. These cubic structures have an $A_2B_2O_7$ format, in which the B-O bond pair is primarily responsible for maintaining structural integrity and elastic properties (Ref 11). In pyrochlores, the B ions are coordinated with six O ions with relatively short B–O bond lengths. In contrast, the A ions are coordinated with eight O ions and have large and weak A–O bonding. Consequently, any weakening of B-O bonding can result in structural relaxation, lattice strain, and potentially higher values of CTE, elastic modulus, and

fracture toughness. A-site elements must be studied in terms of possible interaction with bond coat and topcoat oxidation, and corrosion resistance (Ref 130–132).

As a first step towards choosing rare-earth elements for the A-site, consideration should be given to the TGO layer. Potentially many rare-earth elements can react with Al in a bond coat and produce α-Al_2O_3, but the kinetics, thermodynamics, and thermophysical properties must all be taken into account (Ref 133–135). For example, Leckie *et al.* (Ref 135) declared that by decreasing the Y amount in the topcoat layer and adding Gd, an interface temperature below 1100 ℃ is required for TGO growth. Alternatively, conventional YSZ could be employed as a diffusion barrier layer to maintain an intact TGO layer. Other concepts such as the formation of brittle intermetallic compounds or other oxide layers can affect the durability of the TBC system. Even though the effect of A-site cations on the performance of the TBC and its compatibility with other layers are crucial to our knowledge, no papers have been published on this subject.

The nomenclature of HEOs is based on the elements present at the B-site. When it comes to mixed oxides, multiple transition elements can occupy the B-site position. Accordingly, zirconates incorporate just Zr, aluminates feature Al, cerium oxides contain Ce, hafnates have Hf, and niobates encompass Nb. All of the aforementioned combinations fall under the category of HEOs.

Mixed Oxides

Gild et al. (Ref 86), employed high-energy ball milling for powder mixing, followed by spark plasma sintering and annealing, to synthesize various high entropy fluorite oxides. The single-phase compositions of these synthesized ceramics are detailed in Table 1, rows 2 to 8. Notably, all these compositions displayed low thermal conductivity values and relatively high hardness compared to YSZ samples prepared using the same method. The high entropy oxides exhibited

promising potential due to their low thermal conductivity, attributed to the presence of various cation species, resulting in phonon scattering induced by mass and bonding disorder. For phase stability, Sun *et al.* (Ref 136) found that the compositions could maintain their single-phase solid solution structure up to 1700K, suggesting a lack of precipitation reactions based on the positive values observed for both the second derivative of Gibbs free energy and the Gibbs free energy change of chemical reaction.

Zhao *et al.* (Ref 83) studied the CTE and thermal conductivity of $(Y_{0.25}Yb_{0.25}Er_{0.25}Lu_{0.25})_2(Zr_{0.5}Hf_{0.5})_2O_7$ (Row 9), prepared using spark plasma sintering. They reported that the HEO has low thermal conductivity. This was mainly associated with the high entropy sluggish grain growth effect. Interestingly, its CTE value closely matched that of Al_2O_3, which forms the TGO, making it a promising candidate for environmental barrier coating (EBC). Due to its suitable properties, this HEO may be a preferred choice for TBC topcoats.

Wright *et al.*(Ref 137), synthesized three HEOs as well as two non-equimolar medium entropy oxides, all with general compositions of $(Hf_{1/3}Zr_{1/3}Ce_{1/3})_{1-x}(Y_{1/2}X_{1/2})_xO_{2-\delta}$ (where X=Yb, Ca, and Gd) (Rows 10, 11), and reported their stability up to 1500℃. These materials exhibited lower thermal conductivity values compared to YSZ, attributed to the presence of oxygen vacancies and especially clustering in their microstructure. In this research, to create a uniform mixture of ceramics, a planetary ball mill was employed, followed by spark plasma sintering to achieve dense ceramics.

Song *et al.* (Ref 126), studied the thermophysical and mechanical properties of an HEO synthesized via solid-state reaction with a composition of $(Y_{1/2}Yb_{1/2})_2(Ti_{1/3}Zr_{1/3}Hf_{1/3})_2O_7$ shown in row 12. The study confirmed the expected thermal conductivity and high CTE of the HEO. Besides, high hardness and elastic modulus were reported due to the solid solution hardening

mechanisms, mass disorder, and atomic size differences of A-site and B-site cations. Zhang *et al.* (Ref 100), designed and synthesized an oxide-type high entropy with a composition of $La_2(Zr_{0.2}Ce_{0.2}Hf_{0.2}Sn_{0.2}Ti_{0.2})_2O_7$ using a solid-state reaction method. The composition has been reported to have low thermal conductivity and CTE values (row 13). In comparison to YSZ, thermal conductivity and CTE were lower. Afterward, the HEO powder was granulated and then deposited using air plasma spray technology.

Among all oxide-based high entropy compositions, in which the B-site position is occupied by O, only $La_2(Zr_{0.2}Ce_{0.2}Hf_{0.2}Sn_{0.2}Ti_{0.2})_2O_7$ has been thermally sprayed. The HEO was deposited on a bond coat using the air plasma spray method, with a thickness of 120 μm. SEM images of the cross-section of the coating are given in Figure 2. In terms of the microstructure, as declared by the authors porous coating was formed due to rapid cooling conditions, which resulted in low fracture toughness values. The spray parameters, or particle size distribution, were not mentioned in the reference, which affects the microstructure of the coating. According to the phase analysis results, the initial pyrochlore structure changed into defective fluorite, but it could remain stable at 1100℃ for a long time. Additionally, the authors investigated the performance of the coating during thermal cycling. According to the results, low fracture toughness values led to low performance after cyclic tests at 1050℃.

Recently, Song *et al.* (Ref 138), used the entropy stabilization method to synthesize new compositions (rows 14, 15), with solid-state reactions. The researchers reassembled oxides in the form of $A_2B_2O_7$ or $A_3B'O_7$ to the form of $A_5B_2B'O_{14}$ with a single defective fluorite crystal structure without any secondary phase formations (according to the provided XRD results, given in Figure 3a). In their findings, the researchers reported that the process of reassembling the structure led to an increase in lattice distortion, ultimately leading to lower values of thermal

conductivity. The lattice distortion was verified using the results of Raman spectroscopy, with very broad spectra (given in Figure 3b). Having a high population of cations in these compositions caused the ion sublattice distortion. In terms of thermophysical properties due to the random distribution of multiple cations and oxygen vacancies, the new structure had low thermal conductivity (about 1 W/mK) (Ref 138), while cations and oxygen vacancies in rare-earth zirconates, like intermetallic compounds, are in specific locations. (Ref 77). Also, the composition had a CTE value of ~9.95×10^{-6} 1/K, which is larger than the reported value for $La_2Zr_2O_7$ (8.42×10^{-6} 1/K) (Ref 138). In this research, they used the term HEO for their entropy-stabilized oxides, and the compositions are introduced as promising TBC materials, however, the phase stability and other thermal performances need further investigation.

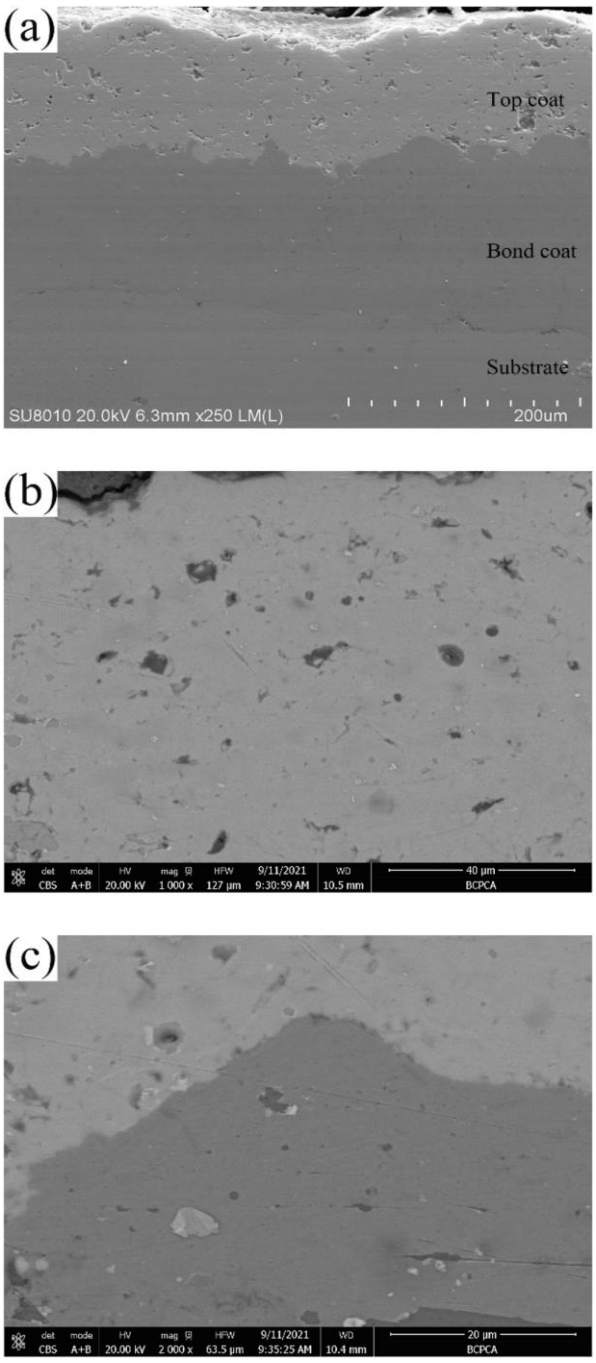

Figure 2- SEM image of as-sprayed TBC with the L(ZCHST)O topcoat. (a) Full view of cross-section SEM image of as-sprayed TBC, (b) topcoat magnification SEM image, (c)interface between topcoat and bond coat magnification SEM image (Ref 100).

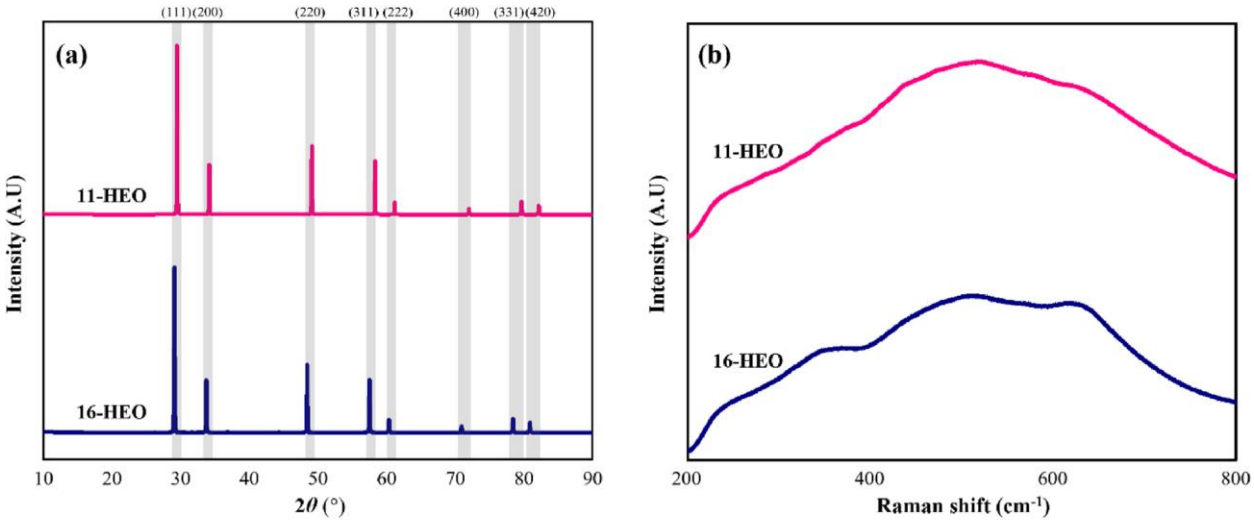

Figure 3: Structural characterization of synthesized ceramics by Song et al., namely (a) XRD patterns, (b) Raman spectrum

Zirconates

High entropy zirconates (HEZ) are a subset of HEOs with Zr occupying the B-site position, typically formulated as $(5RE_{0.2})_2Zr_2O_7$ (rows 16-30). These materials consistently exhibit desirable average values for the critical properties of TBCs and the crystal structure is generally pyrochlore. The choice of Zr in the B-site position, with its relatively large atomic radius (175pm), contributes to an increased cationic ratio. Two novel HEZs were synthesized by Zhao *et. al* (Ref 128), and Luo *et al.* (Ref 139) and shown in rows 16 and 17, Table 1, by co-precipitation method. Both the HEZs demonstrated low thermal conductivity and exceptional thermal stability up to 1600℃ along with excellent sintering resistance. Both groups compared their results with a REZ. High configurational entropy and local ionic charge disorder were reported as the governing factors for decreasing thermal conductivity (Ref 128,139).

However, the fracture toughness values were slightly lower than that of YSZ but higher than REZs (see Table 1). Increased fracture toughness from REZ to HEZ was reported to happen due to severe lattice distortion and their unique microstructure that deflect and branch the microcracks.

Further, the authors found that the crack resistance against thermal stresses increased due to the slow grain growth effect of the HEZ (Ref 128,139). Figure 4a to Figure 4e were published by Zhao et. al (Ref. 99), at different annealing times as evidence of a slower grain growth rate of high entropy zirconate compared to a rare-earth zirconate (with the composition of ($La_2Zr_2O_7$). Their findings revealed that the average grain size of HEZ increased from 1.69 to 3.92 μm, whereas the grain size for REZ changed from 1.96 to 8.89 μm after 18 hours of heat treatment at 1500℃. This demonstrates the potential advantages of HEZs over traditional REZs in TBC applications.

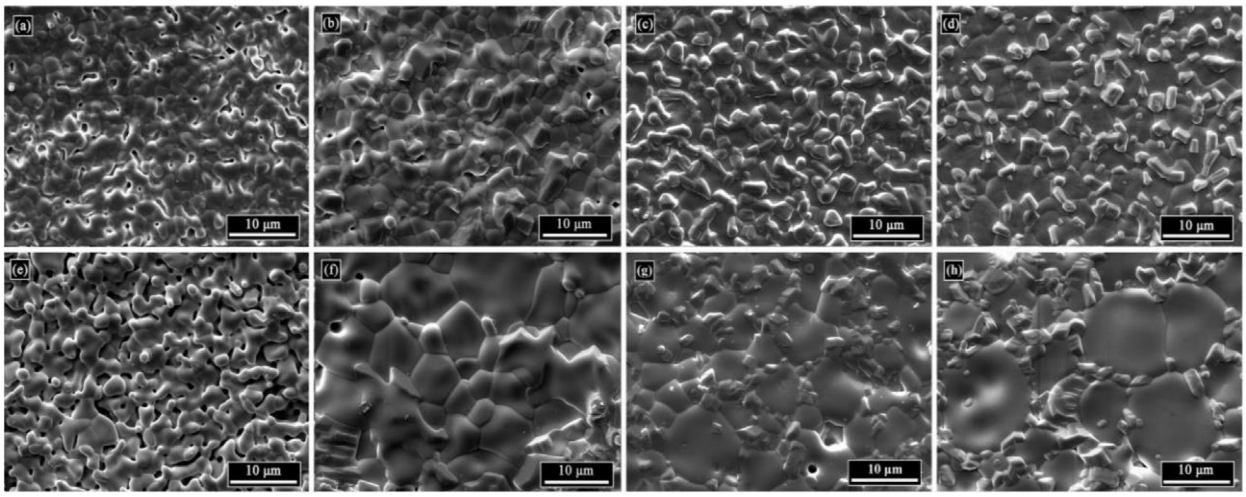

Figure 4: Microstructures of $(La_{0.2}Ce_{0.2}Nd_{0.2}Sm_{0.2}Eu_{0.2})_2Zr_2O_7$and $La_2Zr_2O_7$compacts after annealing at 1500◦C for 1–18 h in the air: ((a): 1 h, (b): 6 h, (c): 12 h, (d): 18 h for$(La_{0.2}Ce_{0.2}Nd_{0.2}Sm_{0.2}Eu_{0.2})_2Zr_2O_7$and (e): 1 h, (f): 6 h, (g): 12 h, (h): 18 h for $La_2Zr_2O_7$); published by Zhao et. al (Ref. 99).

Ren *et al.* (Ref 23), also, studied the thermophysical and mechanical properties of a novel HEZ (row 18), produced by the coprecipitation method; and compared the results with two REZs:

$Sm_2Zr_2O_7$ and $Lu_2Zr_2O_7$. High hardness, fracture toughness, low thermal conductivity, high CTE (close to metals), and thermal stability up to 1400℃ for relatively long durations were reported for the studied HEZ. The study also confirmed the effect of severe lattice distortion on improving the mechanical properties, as well as the cocktail effect on improving thermophysical properties. The latter includes mass differences, severe lattice distortion, and chemical bonding deviation.

Li *et al.* (Ref 93), synthesized five different HEZs by solid-state reaction method, with different lanthanides in the A-site. These HEZs demonstrated exceptionally low thermal conductivity as shown in rows 19-23 of Table 1. Also, their studies on sintering resistance revealed that these ceramics have relatively high sintering resistance. The CMAS corrosion resistance of $(Y_{0.2}Nd_{0.2}Sm_{0.2}Eu_{0.2}Gd_{0.2})_2Zr_2O_7$, (given in row 20) was compared to a REZ ($La_2Zr_2O_7$) reported by Tu *et al.* (Ref 140). Notably, different corrosion mechanisms were observed due to better mechanical properties and reduced crack propagation rates of HEZ. Relatively higher corrosion resistance was also achieved for these HEZs. The point energy-dispersive X-ray spectroscopy (EDS) analyses for these compositions are shown in Figure 5. According to their results, there were no horizontal and vertical cracks in the ceramic substrate and the reaction layer, because of having lower elastic modulus and higher CTE values in HEZs. Also, a fine-grained and dense reaction layer was formed due to the slow diffusion observed in the high-entropy phases. During cooling, this fine-grained reaction layer is expected to enhance the layer's resistance to cracking (Ref 140). Figures 5(c), (d), and (e) display the results of point energy-dispersive X-ray spectroscopy (EDS) analyses of the dark region, rod-shaped crystals, and globular grains. Statistical EDS analysis of multiple regions reveals that rod-shaped crystals are predominantly composed of rare-earth elements (RE), calcium (Ca), and magnesium (Mg), while globular grains are predominantly composed of zirconium (Zr), with small quantities of RE, Ca, and Mg. It is

reported that the dark phase present in the HEZ sample contains substantial quantities of calcium (Ca), magnesium (Mg), aluminum (Al), and silicon (Si). On the other hand, the LZ sample exhibits two types of dark regions, namely an interstitial dark phase and a large "pool" of dark material. The interstitial dark phase and the dark phase in the HEZ sample have similar elemental compositions. While a substantial amount of magnesium and aluminum is present in the dark "pool"(Ref 140). Sun *et al.* (Ref 141) added Alumina to this composition with flash sintering and studied the effect of this addition on the mechanical properties of HEZ. According to these authors, the mechanical properties (including nano-hardness and elastic modulus) were improved due to the formation of perovskite $REAlO_3$ and magnetite $REAl_{11}O_{18}$ phases (Ref 141).

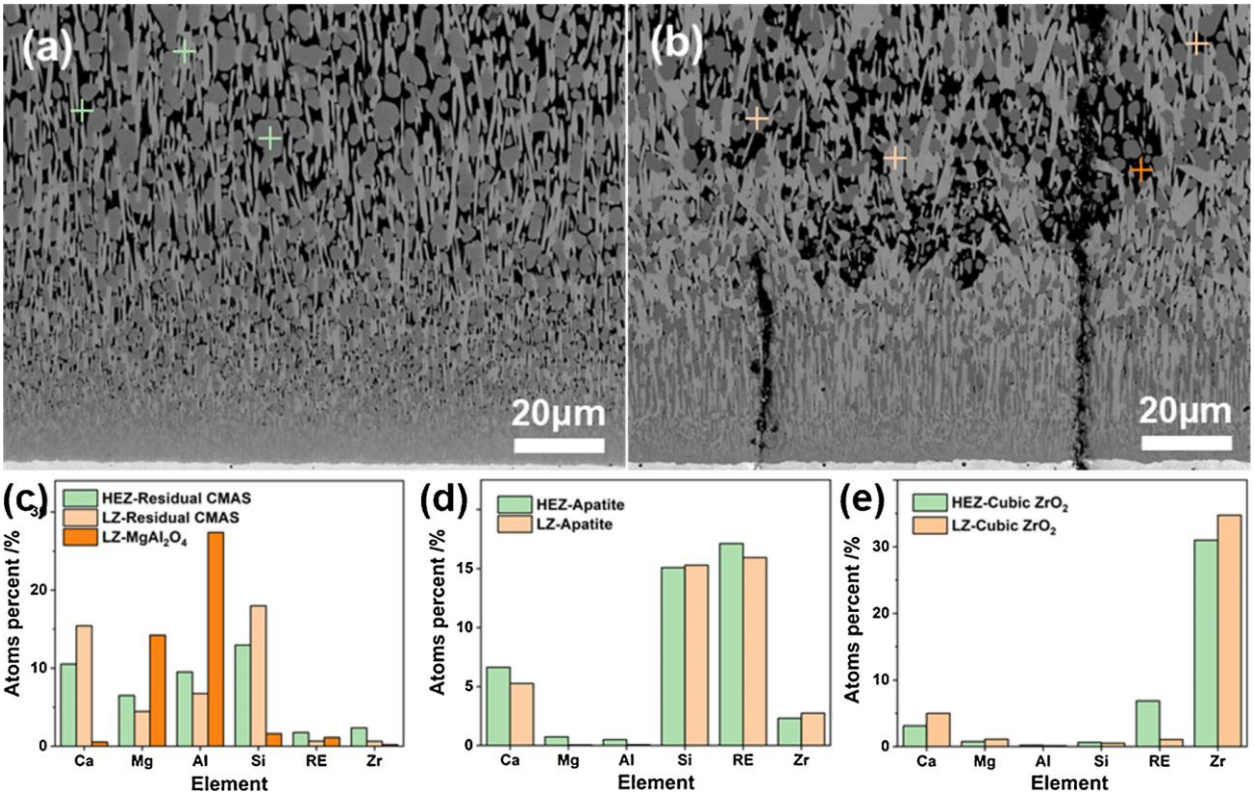

Figure 5: Point EDS analysis results of the CMAS corroded specimens after 24 h corrosion, published by Tu *et al.* (Ref 140). Microstructures of (a) $(La_{0.2}Nd_{0.2}Sm_{0.2}Eu_{0.2}Gd_{0.2})_2Zr_2O_7$ (HEZ) and (b) $La_2Zr_2O_7$ (LZ), element contents of (c) residual CMAS.

Liu *et al.* (Ref 142), and Luo *et al.* (Ref 143), also studied the thermophysical and mechanical properties of a fluorite structure HEZ (row 24). Their results confirmed an acceptable fracture toughness (> 1-2 $MPa.m^{1/2}$) and favorable thermophysical properties of the HEZ composition, primarily driven by the high-entropy effect, cocktail effect (including mass difference), chemical bonding deviation, and local lattice distortion. On the other hand, Luo *et al.* (Ref 143), synthesized two other HEZs (rows 25, 26) using the reverse coprecipitation method, and their results were inconsistent with other materials.

An ultrafine-grained HEZ (row 27) was fabricated by high-pressure sintering of the self-synthesized nano powders, reported by Ma *et al.* (Ref 144). The authors examined its mechanical properties including fracture toughness, hardness, and thermal conductivity. The results were satisfactory in terms of having high hardness and high fracture toughness (very close to YSZ). For this composition, low thermal conductivity was also reported, and the phase stability of the composition was reported as high as 1500℃. All properties were reported as being due to high-entropy and grain-refinement effects. These compositions seem to be a good fit for high-temperature applications such as TBCs.

The differences in the reported properties were associated with atomic radius differences of A-site REs as well as their electronegativity differences. Among studied HEZs, Zhou *et al.* (Ref 129) are the only ones that have thermally sprayed HEZ (row 28), by using APS on top of a YSZ layer, thus, resulting in a DLC topcoat. A cross-section image of the coating is shown in Figure 6, according to which the coating layers are bonded enough to each other, and the reported porosity was about 9.17 ± 0.87 %. Based on the published results of the EDS on the cross-section it seems that all elements are distributed equally in the coating.

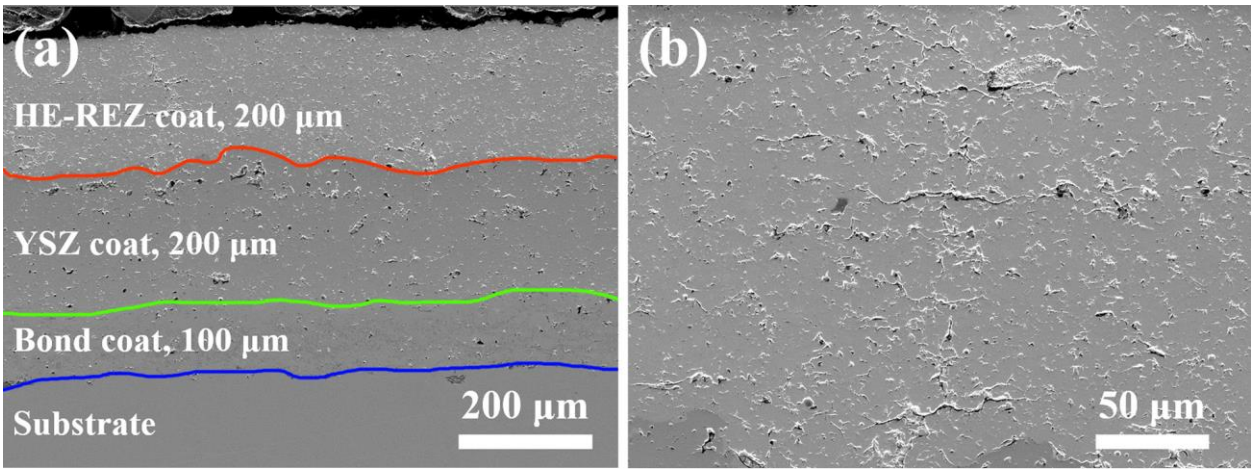

Figure 6: SEM images of the cross-section of (a) the coating system and (b) the $(La_{0.2}Nd_{0.2}Sm_{0.2}Eu_{0.2}Gd_{0.2})_2Zr_2O_7$ ceramic layer published by Zhou *et al.* (Ref 129).

Figure 7 depicts the X-ray diffraction (XRD) spectrum of the high entropy rare earth zirconate (HE-REZ) ceramic coating. The diffraction peaks observed in the as-sprayed $(La_{0.2}Nd_{0.2}Sm_{0.2}Eu_{0.2}Gd_{0.2})_2Zr_2O_7$ (HEZ) ceramic coating can be attributed to a phase-pure defective fluorite structure, without the presence of impurity phases. As indicated in the table, the structure of the HEZ ceramic powder synthesized initially was pyrochlore, which can be regarded as an ordered fluorite structure in the cation sublattices.

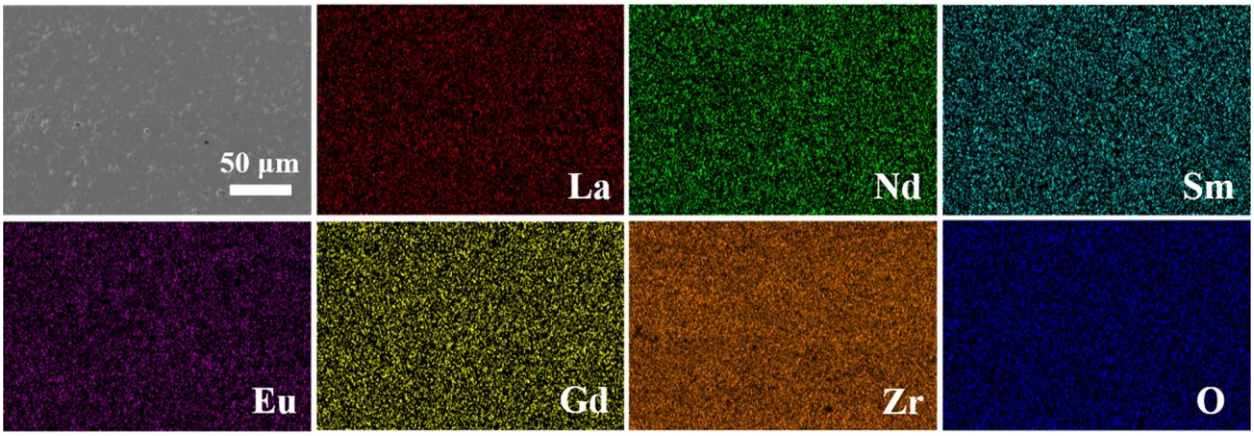

Figure 7: EDS elemental maps on the polished cross-section of the HE-REZ ceramic coating published by Zhou *et al.* (Ref 129).

Zhou *et al.* (Ref 129), examined the thermal cyclic behavior of this DLC at 1100℃ (see Figures 8-10). The authors reported that the HEZ had a higher lifetime compared to a REZ ($La_2Zr_2O_7$), due to their slow grain growth effect and low sintering rate of HEOs. It is critical to note that, since the TGO grows between the bond coat and the topcoat's first layer after TBC operation, it affects the TBC's life. As a result, the TGO should be studied and taken into consideration. In spite of this, this article did not discuss the growth and microstructure of the TGO.

All in all, the spraying of HEZs and the subsequent study on their performance appear to be promising research areas. HEZs emerge as the best candidates for the next generation of TBCs with low thermal conductivity, high CTE, and high fracture toughness. Nonetheless, there is a need for further research into their resistance to erosion and CMAS, which should be addressed. The importance of choosing the appropriate rare-earth elements for A-site cations is emphasized when comparing the reported CTE and thermal conductivity values in the table. The importance of choosing A-site cations is emphasized by comparing the reported CTE and thermal conductivity values. The CTE value is closely related to different lattice energy (U) of ionic crystals, which can

be altered by changing the distance between ions, ionic charges, and the Madelung constant for the crystal lattice or structural coefficient (Ref 145–147). The Madelung constant changes according to the electronegativity value of A-site elements in pyrochlore structures (Ref 148,149). Importantly, increasing U leads to a reduction in CTE (Ref 148–150). Additionally, changing the average atomic mass differences as well as ionic radii differences affect thermal conductivity. Increasing the differences decreases the thermal conductivity value (Ref 150). These emphasize the significance of selecting the most appropriate A-site cations for the specific application.

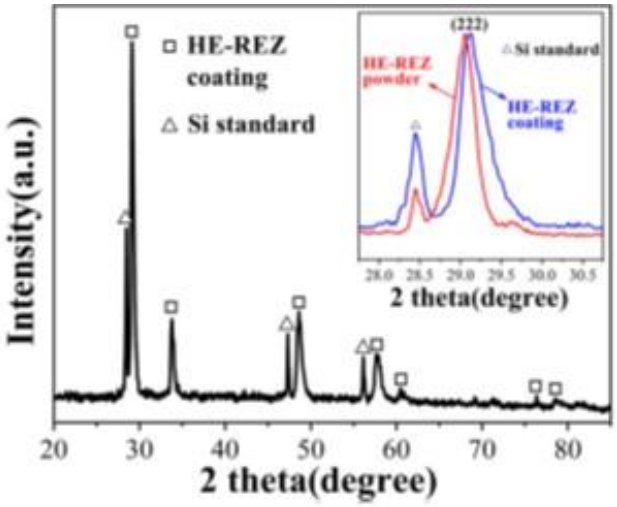

Figure 8: XRD pattern of the as-sprayed HE-REZ ceramic coating. The inset is the zoom-in view of (222) peak compared with that of as-synthesized $(La_{0.2}Nd_{0.2}Sm_{0.2}Eu_{0.2}Gd_{0.2})_2Zr_2O_7$ published by Zhou *et al.* (Ref 129).

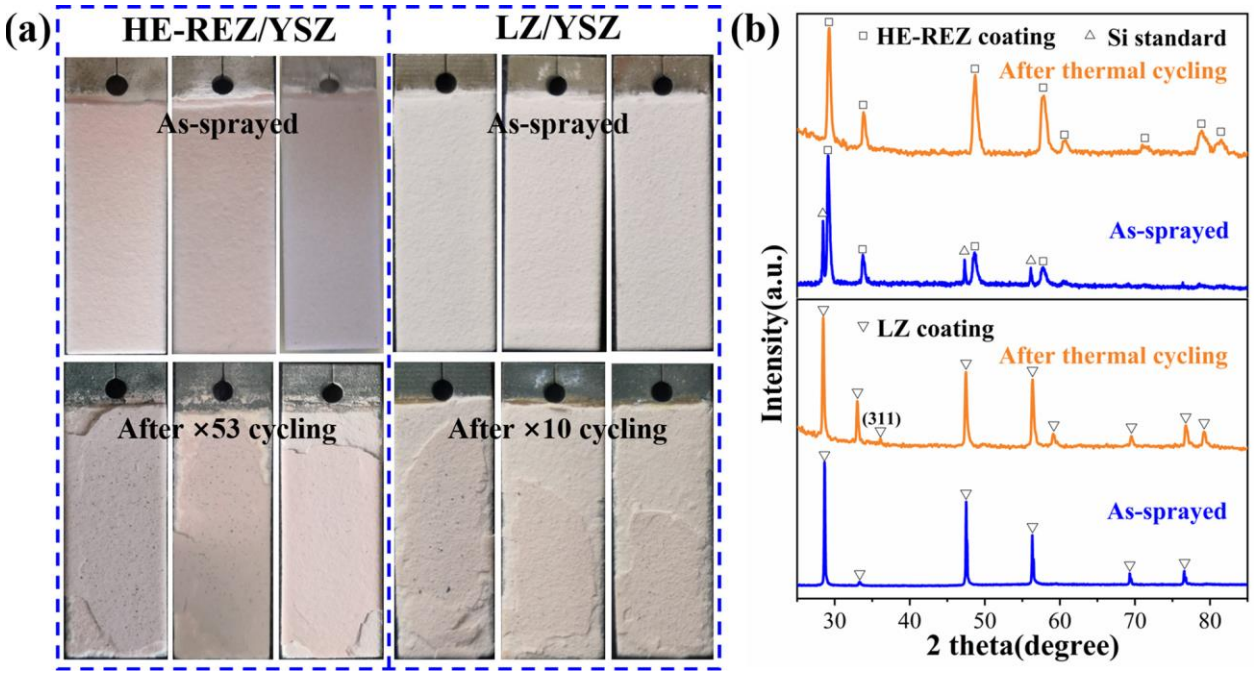

Figure 9: (a) Photographs of the as-sprayed coating and after the thermal cycling test. (b) XRD pattern of the $(La_{0.2}Nd_{0.2}Sm_{0.2}Eu_{0.2}Gd_{0.2})_2Zr_2O_7$ (HE-REZ) ceramic and LZ coating before and after thermal published by Zhou *et al.* (Ref 129).

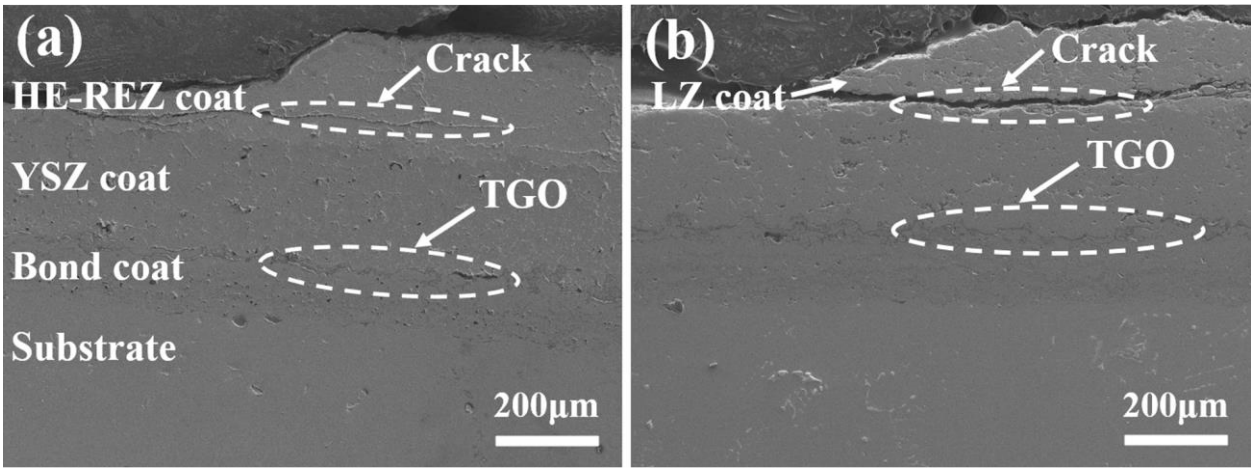

Figure 10: SEM images of the cross-sections of the TBCs after the thermal cycling test. (a) $(La_{0.2}Nd_{0.2}Sm_{0.2}Eu_{0.2}Gd_{0.2})_2Zr_2O_7$ (HE-REZ); (b) $La_2Zr_2O_7$ (LZ) published by Zhou *et al.* (Ref 129).

CMAS resistance of a novel HEZ with a composition of $(Y_{0.2}Gd_{0.2}Er_{0.2}Yb_{0.2}Lu_{0.2})_2Zr_2O_7$, as shown in row 29 of Table 1, has been studied by Deng *et al.* (Ref 151). The composition was synthesized by the solid-state reaction method and spark plasma sintering. Comparing the thermophysical and mechanical properties of the HEZ also revealed that it can be introduced as a promising TBC topcoat. Regarding the CMAS corrosion resistance, as per their statement, the rapid expansion of CMAS on the HEZ pellet facilitates quick reaction and recession layer formation. By forming a recession layer, the material can be protected from further infiltration of CMAS. The details are given in Figure 11.

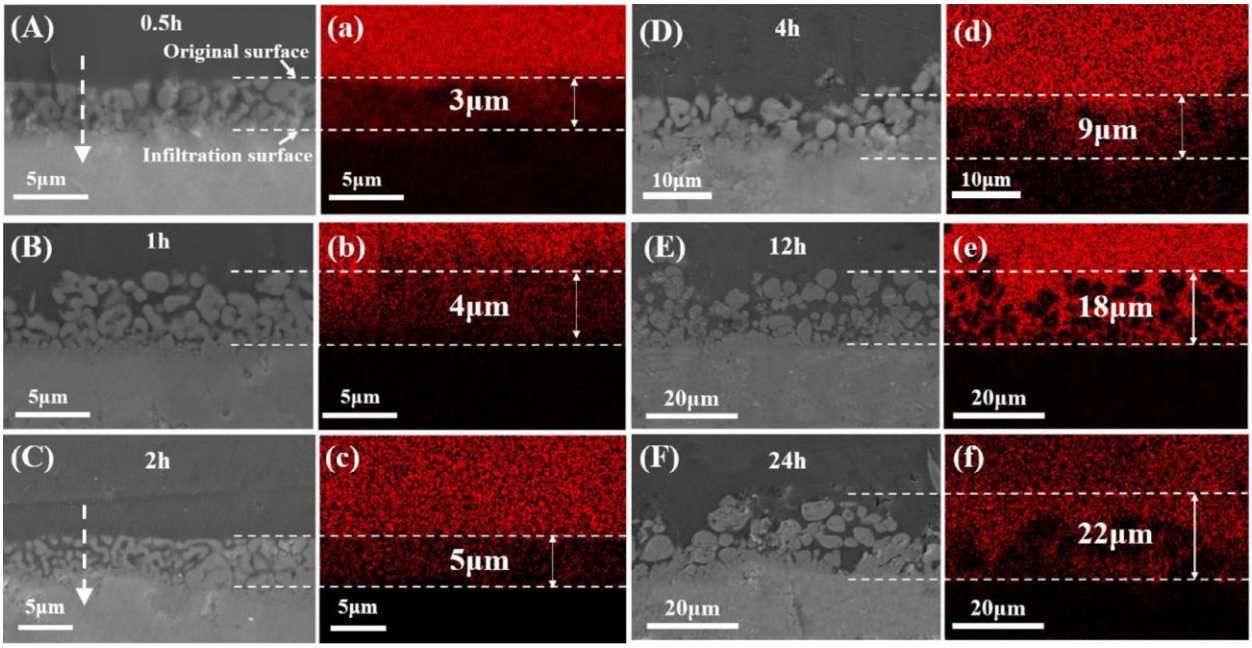

Figure 11: (A-F) The cross-sectional images of CMAS-reacted HE-REZ pellets for 0.5, 1, 2, 4, 12, and 24 h, respectively. (a-f) The corresponding EDS elemental Si maps; published by Deng et al. (Ref 151).

Yan *et al.* (Ref 152), synthesized a fluorite HEZ, by solid-state reaction and high-temperature sintering with a composition of $(Gd_{0.2}Y_{0.2}Er_{0.2}Tm_{0.2}Yb_{0.2})_2Zr_2O_7$, given in row 30 Table 1. They also studied thermophysical and mechanical properties as well as the CMAS corrosion resistance

of the HEZ at 1250℃ and 1300℃ at different times (changing from 0.5 h to 10h). According to their results, HEZ exhibits a similar thermal expansion coefficient to YSZ at high temperatures. This similarity helps to alleviate the issue of thermal stress resulting from a mismatch in thermal expansion coefficients, thereby extending the coating's lifespan. Additionally, HEZ exhibits very low thermal conductivity, and high fracture toughness, highlighting its strong potential as a promising material for TBC applications.

Luo *et al.* (Ref 153) prepared a HEZ by reverse co-precipitation process, with a composition of $(Dy_{0.2}Nd_{0.2}Sm_{0.2}Eu_{0.2}Yb_{0.2})_2Zr_2O_7$ given in row 31 of Table 1. As a result of the slow diffusion phenomenon, the HEZ demonstrated excellent sintering resistance. Even after annealing at 1600°C for 1 to 50 hours, the average grain size increased, from 0.73 to 2.22 μm. The researchers concluded that HEZ shows high potential as a ceramic material for TBCs, offering excellent anti-sintering properties, high fracture toughness, a large CTE, and low thermal conductivity.

Cerium Oxides

Adding cerium oxide to YSZ (CSZ or CYSZ) has been reported to enhance corrosion resistance and fracture toughness and decrease thermal conductivity (Ref 154–156). Rare-earth cerium oxides with a composition of $RE_2Ce_2O_7$ are proposed as new TBC topcoats, as their thermophysical properties are improved compared to CYSZ or CSZ (Ref 157,158). High entropy cerium oxides with compositions of $(5RE_{0.2})_2Ce_2O_7$ show greater CTE than that of YSZ close to Ni-based superalloys, as well as high-temperature stability, which is desirable for topcoats (rows 32-41). All synthesized HEOs with Ce in the B-site are stabilized in a fluorite structure.

Tang *et al.* (Ref 159), designed and synthesized two high-entropy cerium oxides, and studied their thermophysical properties. Lilin *et al.* (Ref 160) also studied the CTE and thermal conductivity of an HEO with Ce in the B-site (rows 23). Their studies reported that the higher CTE of the composition is mainly attributed to the weak bonding between Ce cations and O anions, as well as their low thermal conductivity, which resulted from phonon scattering due to the lattice distortion effect. Another HEO was fabricated by Zhang *et al.* (Ref 161), which also showed high CTE and low thermal conductivity. The values were compared to that of $Sm_2Ce_2O_7$. The hardness and fracture toughness of high entropy cerium oxide were also investigated. This is the only study of the mechanical properties of high entropy cerium oxide conducted to date. However, HEZs appear to be more efficient in terms of mechanical performance than high-entropy cerium oxides. All ceramics mentioned here had a thermal stability of 1200℃, which is not significantly higher than YSZ. Xu *et al.* (Ref 84,162), synthesized six other compounds with thermophysical properties that were suitable and have phase stability up to 1600℃ (rows 37 -41). This highlights the importance of selecting the proper cations for A-sites. On the other hand, their mechanical properties currently remain unknown.

Other High Entropy Oxides

Aluminates

A novel high entropy aluminate was developed by Chen *et al.* (Ref 163) as shown in row 42 of the table. The HEO was prepared using the solid-state reaction method and SPS. Having a CTE value close to Al_2O_3, ceramic makes it a viable topcoat choice. Additionally, the ceramic has low thermal

conductivity, high sintering resistance, and is very stable at high temperatures, since it possesses all high entropy core effects.

However, it's important to note that further investigation based on the mechanical properties has yet to be performed and almost no other data has been found for high entropy aluminates. Notably, in the available references and literature, limited data regarding new high entropy aluminates has been found. Authors have not reported further information or studies on high entropy aluminates, which underscores the need for more comprehensive research in this particular field to uncover their full range of properties and potential applications.

Hafnates

Unlike HEZs, limited data is available for high entropy hafnates. A comparison between Hafnates and Zirconates indicates that Hafnates exhibit superior phase stability at high temperatures, a lower volume change due to phase transitions, and lower thermal conductivity (Ref 148,164). Cong *et al.* (Ref 165,166) synthesized two compositions with fluorite structure which was stable up to 1600℃ and showed favorable thermophysical properties compared to YSZ. Compositions are given in rows 43 and 44 of Table 1. The interesting point is that the compositions are chemically compatible with Al_2O_3 at 1300℃, which makes them a good choice for TBCs and EBCs.

Ye *et al.* (Ref 167) prepared an entropy-stabilized Hafnate with the composition of $(Y_{0.2}Dy_{0.2}Er_{0.2}Tm_{0.2}Yb_{0.2})_4Hf_3O_{12}$, by the emerging ultrafast high-temperature sintering (UHS) method. In their study of the CMAS corrosion resistance, morphological changes have been studied. The results at different times of corrosion testing are given in Figure 12. It appears that the thickness of the reaction layer has increased by increasing time, which may be explained by

the structural change in the layer. Based on the published results, this Hafnate has an acceptable corrosion resistance as a result of the formation of a dense structure layer, which acts as a barrier to the penetration of molten CMAS into the ceramic material. In addition, the small radius of the rare-earth ions and the Ca^{2+} accounts for the slow reaction rate. There has been no investigation of the phase stability of the Hafnate or its behavior during thermal spraying.

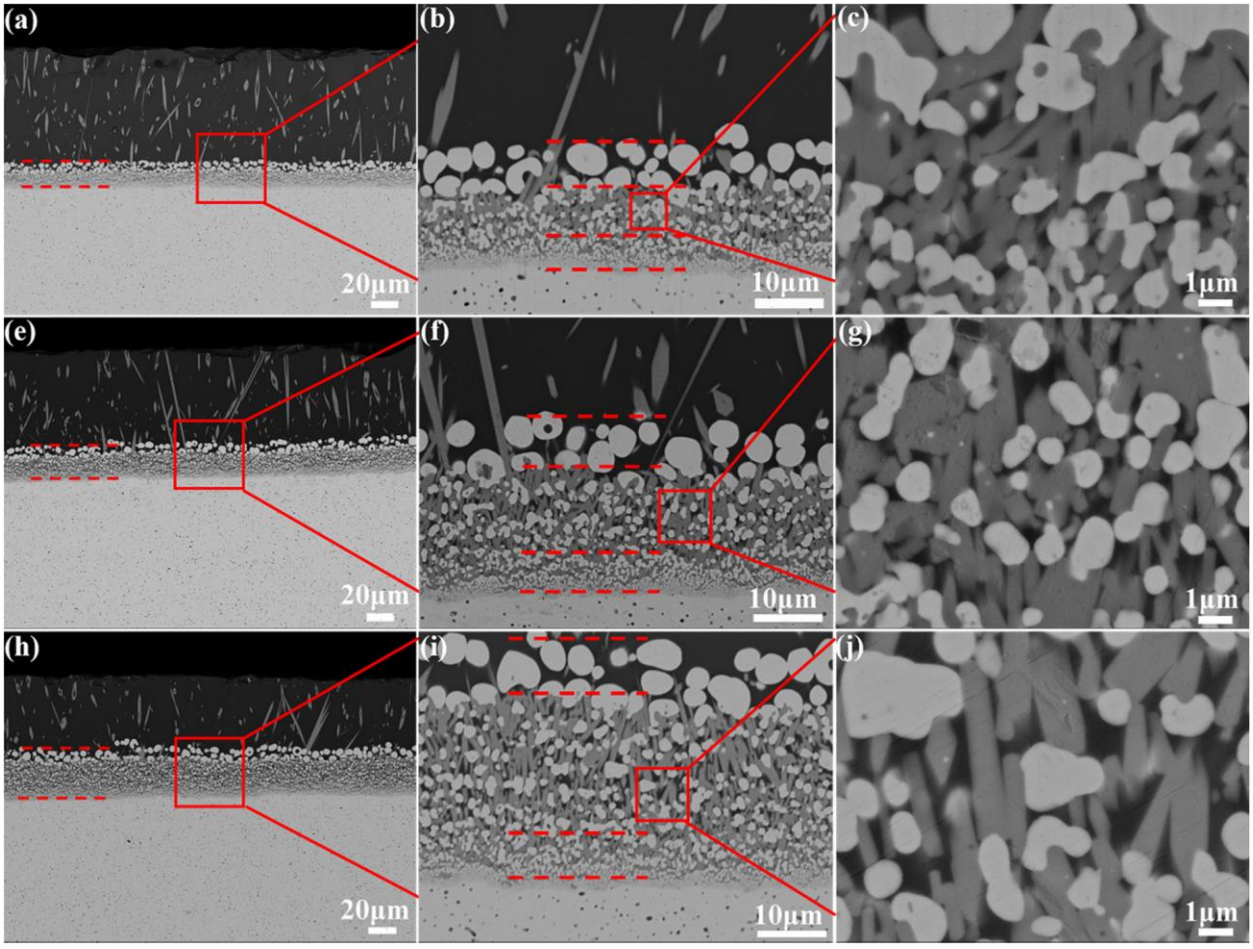

Figure 12: Cross-sectional morphologies (BSE) of 5YH after molten CMAS corrosion at 1300 ℃ for 5 h (a, b and c), 7.5 h (d, e and f), and 10 h (h, i and j) published by Ye et al. (Ref 167).

Niobates

Zhu *et al.* (Ref 168) designed and synthesized a $(5RE_{0.2})_3NbO_7$ ceramic with high configurational entropy, shown in row 45 of Table 1. The composition was synthesized via solid-state reaction as a result of the cocktail effect, lattice distortions, and oxygen vacancies, the ceramic has a very low thermal conductivity. The high fracture toughness was reported to happen due to the grain refinement effect of high entropy. As shown by the present properties of the bulk of this HEO, it appears to be a potential candidate for the next generation of TBC topcoats.

Zhao *et al.* (Ref 169), synthesized two other high entropy Niobates using the solid-state reaction method, (rows 46 and 47 of the table) with the chemical composition of $(Y_{1/3}Yb_{1/3}Er_{1/3})_3NbO_7$, and $(Sm_{1/6}Eu_{1/6}Y_{1/6}Yb_{1/6}Lu_{1/6}Er_{1/6})_3(Nb_{1/2}Ta_{1/2})O_7$. The compositions had a defective fluorite structure. The thermal expansion coefficient, phase stability, and chemical compatibility of the compositions with TGO (α-Al_2O_3 powder) were compared to rare-earth Niobates (RE_3NbO_7, RE: Y, Yb, Er, SM, Eu). Based on their findings these high entropy compositions and rare-earth niobates seemed to be stable up to 1250℃. Results of chemical compatibility with α-Al_2O_3 also show that the studied ceramics don't react with TGO, but according to Figure 13, increasing the temperature to 1300℃, caused the formation of new oxides. Considering the current working temperature of TBCs, the high entropy Niobates could be a candidate as a topcoat, while for the increased gas turbine operation temperatures, the stability and compatibility should be improved. Based on published articles, no high entropy Niobate coatings have been investigated till now.

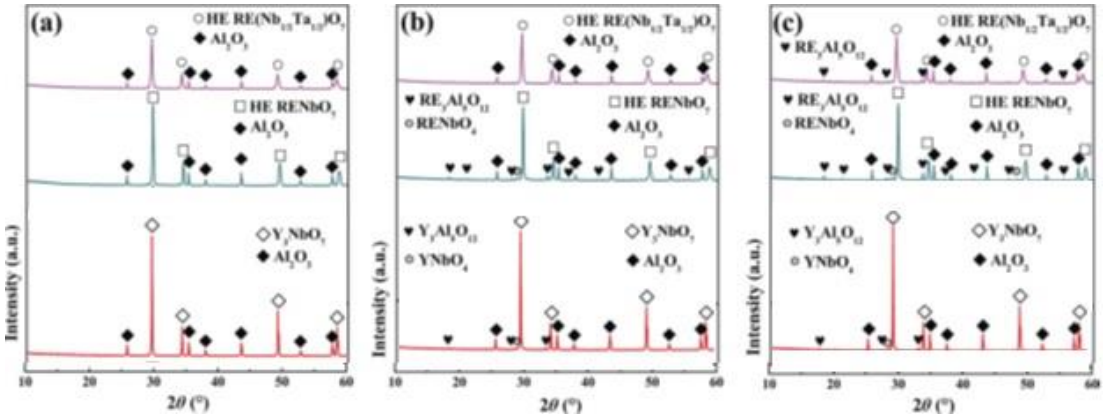

Figure 13: XRD patterns of the mixed powders of Y_3NbO_7, HE RE_3NbO_7, HE $RE_3(Nb_{1/2}Ta_{1/2})O_7$, and α-$Al_2O_3$ after annealing at different temperatures for 2 h: (a) 1200 ℃, (b) 1250 ℃, and (c) 1300 ℃ published by Zhao et al. (Ref 169).

Future Aspects

The future prospects of HEOs for TBC applications appear to be promising in many respects. Firstly, there is a need for focused efforts in designing HEOs, specifically tailored for TBC purposes. This involves exploring various compositions, elemental combinations, and microstructural designs to optimize properties such as thermal conductivity, thermal expansion coefficient (CTE), resistance to CMAS, mechanical properties, and sintering resistance. Through systematic experimentation and advanced computational modeling techniques, researchers can develop HEOs with enhanced performance and tailored properties. This will meet TBC applications' demanding requirements.

Moreover, the integration of artificial intelligence (AI) methods and data-driven approaches can accelerate the discovery and optimization of HEOs for TBCs. AI algorithms can help predict and screen material properties, identify key compositional factors, and optimize processing parameters to achieve desired characteristics. Currently, very limited data is available, as discussed.

HEOs for TBC applications present exciting opportunities for advanced engineering systems such as gas turbines and aero engines. Although the initial costs of developing and implementing novel materials may be considerable, the long-term benefits outweigh the expenses. With their low thermal conductivity, high CTE, potential enhanced resistance to CMAS, and remarkable anti-sintering properties, HEOs have the potential to enable these systems to operate at higher temperatures, enhanced efficiency, and reduced fuel consumption. By providing superior thermal insulation, minimizing thermal stresses, and enhancing durability, these materials can contribute to more efficient and sustainable energy generation. Further research and optimization efforts are necessary to fully exploit the advantages of HEOs as TBCs, but the potential benefits for gas turbines, aero engines, and similar applications are significant.

On the other hand, HEOs have primarily been studied in bulk ceramic form and in terms of their thermophysical properties. Future research is expected to emphasize the crucial mechanical properties of TBC topcoats, such as fracture toughness and elastic modulus. Understanding these mechanical properties is essential for determining the suitability of HEOs in TBC applications and ensuring their long-term performance and durability. The behavior of these HEOs during the thermal spraying process is also expected to be of increasing interest. In addition, they will be evaluated in terms of their performance as topcoats for TBC. Such research will provide valuable insights into the feasibility and effectiveness of HEOs in practical TBC systems. In particular, it will address their deposition mechanism, coating formation, adhesion, coherence, and thermal cycling resistance challenges.

Summary

Developing improved TBC systems may be accomplished by enhancing the properties of the topcoat ceramic, which faces aggressive thermal and mechanical stresses in GTs. High entropy oxides (HEOs) have recently emerged as a novel class of materials with promising and unique properties that can be tailored for various applications. This review highlighted the remarkable properties of HEOs in the context of TBCs. Their low thermal conductivity, high phase stability (higher than 1200 °C), and high thermal expansions (often close to metallic substrates or bond coats) make them attractive candidates for TBC ceramics. While the published data regarding mechanical properties such as toughness and hardness is very limited, zirconates have been found to perform better in the face of damage or thermo-mechanical shocks.

Beyond the material choice, there are still several aspects to explore when considering HEOs as TBC topcoats. These include their interactions with the bond coat, their mechanical properties, and their ability to perform under erosive and corrosive conditions. Since HEOs are synthesized in pyrochlore or defective fluorite structures, they may undergo phase transformations from pyrochlore to defective fluorite structure during TS or even during coating operation. Also, researchers have rarely deposited HEOs and studied the microstructure of the coating and coating's hot corrosion resistance (CMAS specifically) which reduces the lifetime of TBCs. Furthermore, no information was found regarding the erosion resistance of HEOs. These gaps highlight the importance of continuing to characterize HEOs as TBC topcoats.

All in all, using HEOs as TBC topcoats presents a promising approach to enabling GTs to operate at higher temperatures, and therefore with improved efficiency. Nevertheless, further investigation is still required to elucidate the mechanical properties of these materials while being processed (thermal spraying) and in operation (corrosion or CMAS resistance, etc.). Finally, based on the

reviewed data, the authors express the belief that further investigation into these high entropies is essential.

Acknowledgments

This work was conducted as part of the project titled Engineering the Next Generation of Thermal Barrier Coatings (TBCs) Via Thermal Spraying, supported by the National Research Council of Canada (NRC) Surftec Industrial R&D Group, as well as, the NRC's National Program Office. The authors would like to acknowledge the NRC, as well as, the Surftec Industrial R&D Group members that supported this investigation and publication, the Consortium de recherche et d'innovation en transformation métallique (CRITM) for funding through its Support Program for Research and Innovation Organizations (PSO), and NRC's academic collaborator to this project, Concordia University.

1 Table 1: Properties of HE ceramics introduced as promising TBC topcoat ceramic

No.	HEO	Structure	thermal conductivity (W/mK)		CTE ($\times 10^{-6}$ K^{-1})		Phase stability (℃)		Fracture Toughness ($MPa.m^{1/2}$)		
1	Conventional Bulk 6-8 wt.% YSZ	-	2.6	(Ref 1)	11.0	(Ref 1)	-	-	~3	Not Given	(Ref 2)
2	$(Hf_{0.25}Zr_{0.25}Ce_{0.25}Y_{0.25})O_{2-\delta}$	F	1.74	(Ref 3)	-	-	-	-	-	-	-
3	$(Hf_{0.25}Zr_{0.25}Ce_{0.25})(Y_{0.125}Yb_{0.125})O_{2-\delta}$	F	1.55	(Ref 3)	-	-	-	-	-	-	-
4	$(Hf_{0.2}Zr_{0.2}Ce_{0.2})(Y_{0.2}Yb_{0.2})O_{2-\delta}$	F	1.29	(Ref 3)	11.6	(Ref 4)	1500	(Ref 5,6)	-	-	-
5	$(Hf_{0.25}Zr_{0.25}Ce_{0.25})(Y_{0.125}Gd_{0.125})O_{2-\delta}$	F	1.17	(Ref 86)	-	-	-	-	-	-	-
6	$(Hf_{0.2}Zr_{0.2}Ce_{0.2})(Y_{0.2}Gd_{0.2})O_{2-\delta}$	F	1.61	(Ref 86)	-	-	-	-	-	-	-
7	$(Hf_{0.25}Zr_{0.25}Ce_{0.25})(Yb_{0.125}Gd_{0.125})O_{2-\delta}$	F	1.81	(Ref 86)	-	-	-	-	-	-	-
8	$(Hf_{0.2}Zr_{0.2}Ce_{0.2})(Yb_{0.2}Gd_{0.2})O_{2-\delta}$	F	2.02	(Ref 86)	-	-	-	-	-	-	-
9	$(Y_{0.25}Yb_{0.25}Er_{0.25}Lu_{0.25})_2(Zr_{0.5}Hf_{0.5})_2O_7$	F	1.4	(Ref 83)	8.9	(Ref 83)	-	-	-	-	-
10	$(Hf_{0.284}Zr_{0.284}Ce_{0.284}Y_{0.074}Yb_{0.074})O_{2-\delta}$	F	1.5	(Ref 137)	12.2	(Ref 137)	1500	(Ref 137)	-	-	-
11	$(Hf_{0.314}Zr_{0.314}Ce_{0.314}Y_{0.029}Yb_{0.029})\ O_{2-\delta}$	F	1.8	(Ref 137)	11.4	(Ref 137)	1500	(Ref 137)	-	-	-
12	$(Y_{1/2}Yb_{1/2})_2(Ti_{1/3}Zr_{1/3}Hf_{1/3})_2O_7$	F	-	-	10.1	(Ref 126)	-	-	2.0	$K_{IC} = 5.1636 H_v . a^2 . c^{-1/}$	(Ref 126)
13	$La_2(Zr_{0.2}Ce_{0.2}Hf_{0.2}Sn_{0.2}Ti_{0.2})_2O_7$	P	-	-	7.5	(Ref 100)	1050	(Ref 100)	-	-	-
14	$(Dy_{0.2}Y_{0.2}Ho_{0.2}Er_{0.2}Yb_{0.2})_5(Ti_{0.25}Zr_{0.25}Ce_{0.25}Hf_{0.25})_2(Nb_{0.5}Ta_{0.5})O_{14}$	F	1.26	(Ref 138)	9.61	(Ref 138)	-	-	-	-	-
15	$(La_{0.1}Nd_{0.1}Sm_{0.1}Eu_{0.1}Gd_{0.1}Dy_{0.1}Y_{0.1}Ho_{0.1}Er_{0.1}Yb_{0.1})_5(Ti_{0.25}Zr_{0.25}Ce_{0.25}Hf_{0.25})_2(Nb_{0.5}Ta_{0.5})O_{14}$	F	1.06	(Ref 138)	9.95	(Ref 138)	-	-	-	-	-
16	$(Yb_{0.2}Nd_{0.2}Sm_{0.2}Eu_{0.2}Gd_{0.2})_2Zr_2O_7$	P	1.0	(Ref 139)	10.5	(Ref 139)	1600	(Ref 139)	1.8	$K_{IC} = \delta(\frac{E}{H_v})^{1/2}\frac{F}{c^{3/2}}$	(Ref 139)
17	$(La_{0.2}Ce_{0.2}Nd_{0.2}Sm_{0.2}Eu_{0.2})_2Zr_2O_7$	P	0.8	(Ref 128)	11.0	(Ref 128)	1600	[57, 58]	1.38		(Ref 139)
18	$(Sm_{0.2}Eu_{0.2}Tb_{0.2}Dy_{0.2}Lu_{0.2})_2Zr_2O_7$	P	0.9-1.5	(Ref 23)	11.0	(Ref 23)	1400	(Ref 23)	2.2		(Ref 23)
19	$(La_{0.2}Nd_{0.2}Sm_{0.2}Eu_{0.2}Y_{0.2})_2Zr_2O_7$	P	0.7-1	(Ref 93)	-	-	1300	(Ref 93)	-	-	-
20	$(Y_{0.2}Nd_{0.2}Sm_{0.2}Eu_{0.2}Gd_{0.2})_2Zr_2O_7$	P	0.7-1.0	(Ref 93)	11.0	(Ref 140)	1300	(Ref 93)	-	-	-
21	$(La_{0.2}Y_{0.2}Sm_{0.2}Eu_{0.2}Gd_{0.2})_2Zr_2O_7$	P	0.95-1.0	(Ref 93)	-	-	1300	(Ref 93)	-	-	-
22	$(La_{0.2}Nd_{0.2}Y_{0.2}Eu_{0.2}Gd_{0.2})_2Zr_2O_7$	P	0.8-0.9	(Ref 93)	-	-	1300	(Ref 93)	-	-	-
23	$(La_{0.2}Nd_{0.2}Sm_{0.2}Y_{0.2}Gd_{0.2})_2Zr_2O_7$	P	0.6-0.9	(Ref 93)	-	-	1300	(Ref 93)	-	-	-
24	$(La_{0.2}Nd_{0.2}Sm_{0.2}Yb_{0.2}Gd_{0.2})_2Zr_2O_7$	F	0.9-1.72	(Ref 142,143)	10.9	(Ref 142,143)	1500	(Ref 143)	2.5	$K_{IC} = \delta(\frac{E}{H_v})^{1/2}\frac{F}{c^{3/2}}$	(Ref 142,143)
25	$(La_{0.2}Sm_{0.2}Eu_{0.2}Gd_{0.2}Yb_{0.2})_2Zr_2O_7$	F	1.3	(Ref 143)	-	-	1500	(Ref 143)	1.7		(Ref 143)
26	$(La_{0.2}Nd_{0.2}Eu_{0.2}Gd_{0.2}Yb_{0.2})_2Zr_2O_7$	F	1.5	(Ref 143)	-	-	1500	(Ref 143)	1.6		(Ref 143)
27	$(Sm_{0.2}Gd_{0.2}Dy_{0.2}Er_{0.2}Yb_{0.2})_2Zr_2O_7$	F	1.6	(Ref 144)	-	-	-	-	3.4		(Ref 144)

No.	HEO	Structure	thermal conductivity (W/mK)		CTE ($\times 10^{-6}$ K^{-1})		Phase stability (℃)		Fracture Toughness (MPa.m$^{1/2}$)		
28	$(La_{0.2}Nd_{0.2}Sm_{0.2}Eu_{0.2}Gd_{0.2})_2Zr_2O_7$	P	-	-	10.7	(Ref 129)	-	-	1.1		(Ref 129)
29	$(Y_{0.2}Gd_{0.2}Er_{0.2}Yb_{0.2}Lu_{0.2})_2Zr_2O_7$	P	< 0.9	(Ref 151)	10.2	(Ref 151)	1600	(Ref 151)	-	-	-
30	$(Gd_{0.2}Y_{0.2}Er_{0.2}Tm_{0.2}Yb_{0.2})_2Zr_2O_7$	F	1.2	(Ref 152)	9.9	(Ref 152)	-	-	1.53	$K_{IC} = \delta(\frac{E}{H_v})^{1/2}\frac{F}{c^{3/2}}$	(Ref 152)
31	$(Dy_{0.2}Nd_{0.2}Sm_{0.2}Eu_{0.2}Yb_{0.2})_2Zr_2O_7$	P	1.2	(Ref 153)	-	-	1600	(Ref 153)	2.07		(Ref 153)
32	$(La_{0.2}Nd_{0.2}Yb_{0.2}Y_{0.2}Sm_{0.2})_2Ce_2O_7$	-	1.8-2.4	(Ref 159)	8.0	(Ref 159)	1200	(Ref 159)	-	-	-
33	$(La_{0.2}Nd_{0.2}Yb_{0.2}Y_{0.2}Lu_{0.2})_2Ce_2O_7$	F	1.2-1.8	(Ref 159)	9.0	(Ref 159)	1200	(Ref 159)	-	-	-
34	$(La_{0.25}Sm_{0.25}Gd_{0.25}Yb_{0.25})_{22}Ce_2O_7$	F	1.8-2.5	(Ref 160)	12.0	(Ref 160)	1200	(Ref 160)	-	-	-
35	$(La_{1/6}Nd_{1/6}Yb_{1/6}Y_{1/6}Sm_{1/6}Lu_{1/6})_2Ce_2O_7$	F	1.1-1.6	(Ref 161)	8.5	(Ref 161)	1200	(Ref 161)	1.9	Not Given	(Ref 161)
36	$(La_{0.2}Sm_{0.2}Er_{0.2}Yb_{0.2}Y_{0.2})_2Ce_2O_7$	F	1.3-1.8	(Ref 162)	11.9	(Ref 162)	1700	(Ref 162)	-	-	-
			1.5	(Ref 84)	12.1	(Ref 84)	1600	(Ref 84)		-	
37	$(La_{0.2}Nd_{0.2}Sm_{0.2}Gd_{0.2}Y_{0.2})_2Ce_2O_7$	F	1.5	(Ref 84)	11.9	(Ref 84)	1600	(Ref 84)	-	-	-
38	$(La_{0.2}Nd_{0.2}Gd_{0.2}Er_{0.2}Yb_{0.2})_2Ce_2O_7$	F	1.5	(Ref 84)	12.0	(Ref 84)	1600	(Ref 84)	-	-	-
39	$(La_{0.2}Gd_{0.2}Er_{0.2}Yb_{0.2}Y_{0.2})_2Ce_2O_7$	F	1.5	(Ref 84)	11.9	(Ref 84)	1600	(Ref 84)	-	-	-
40	$(Gd_{0.2}Dy_{0.2}Er_{0.2}Yb_{0.2}Y_{0.2})_2Ce_2O_7$	F	1.5	(Ref 84)	11.9	(Ref 84)	1600	(Ref 84)	-	-	-
41	$(Sc_{0.2}Er_{0.2}Gd_{0.2}Yb_{0.2}Lu_{0.2})_2Ce_2O_7$	F	1.3	(Ref 84)	-	-	1600	(Ref 84)	-	-	-
42	$(Y_{0.2}Yb_{0.2}Lu_{0.2}Eu_{0.2}Er_{0.2})_3Al_5O_{12}$	-	2.4-3.6	(Ref 163)	-	-	1600	(Ref 163)	-	-	(Ref 163)
43	$(Y_{0.2}Gd_{0.2}Dy_{0.2}Er_{0.2}Yb_{0.2})_2Hf_2O_7$	F	0.9-1.0	(Ref 166)	10.6	(Ref 166)	1700	(Ref 166)	-	-	-
44	$(La_{0.2}Ce_{0.2}Pr_{0.2}Sm_{0.2}Eu_{0.2})_2Hf_2O_7$	P	1.0	(Ref 165)	12.7	(Ref 165)	1600	(Ref 165)	-	-	-
45	$(Dy_{0.2}Ho_{0.2}Er_{0.2}Y_{0.2}Yb_{0.2})_3NbO_7$	F	0.7	(Ref 168)	10.2	(Ref 168)	-	-	2.1	-	(Ref 168)
46	$Y_{1/3}Yb_{1/3}Er_{1/3})_3NbO_7$	F	-	(Ref 169)	10	-	-	-	-	-	-
47	$(Sm_{1/6}Eu_{1/6}Y_{1/6}Yb_{1/6}Lu_{1/6}Er_{1/6})_3(Nb_{1/2}Ta_{1/2})O_7$	F	-	(Ref 169)	7	-	-	-	-	-	-

* Note that in the table δ is a constant coefficient, E is Young's modulus, H_v is Vickers hardness, F is the indentation load, and c is distance from the center of indentation to the tip of the crack.

* All reported values for thermal conductivity and CTE are given at 1000℃.

References

1. R. Vaßen, M.O. Jarligo, T. Steinke, D.E. Mack, and D. Stöver, Overview on Advanced Thermal Barrier Coatings, *Surf Coat Technol*, 2010, **205**(4), p 938–942.

2. J. He, Advanced MCrAlY Alloys with Doubled TBC Lifetime, *Surf Coat Technol*, Elsevier B.V., 2022, **448**, p 128931.

3. C.U. Hardwicke and Y.C. Lau, Advances in Thermal Spray Coatings for Gas Turbines and Energy Generation: A Review, *Journal of Thermal Spray Technology*, 2013, **22**(5), p 564–576.

4. M.I. Boulos, P.L. Fauchais, and J.V.R. Heberlein, "Thermal Spray Fundamentals From Powder to Part Second Edition," 2021.

5. D.R. Clarke, M. Oechsner, and N.P. Padture, Thermal-Barrier Coatings for More Efficient Gas-Turbine Engines, *MRS Bull*, 2012, **37**(10), p 891–898.

6. N. Rudrapatna, B. Lutz, and H. Kington, Next Generation Aps Porous Tbc for Gas Turbine Combustors, *J Eng Gas Turbine Power*, 2022, **145**(4), doi:10.1115/1.4055919.

7. I. Gurrappa and a. Sambasiva Rao, Thermal Barrier Coatings for Enhanced Efficiency of Gas Turbine Engines, *Surf Coat Technol*, 2006, **201**(6), p 3016–3029, doi:10.1016/j.surfcoat.2006.06.026.

8. R. Vaßen, E. Bakan, D.E. Mack, and O. Guillon, A Perspective on Thermally Sprayed Thermal Barrier Coatings: Current Status and Trends, *Journal of Thermal Spray Technology*, Springer, 2022, **31**(4), p 685–698.

9. Z. Yan, B. Gainey, J. Gohn, D. Hariharan, J. Saputo, C. Schmidt, F. Caliari, S. Sampath, and B. Lawler, "The Effects of Thick Thermal Barrier Coatings on Low-Temperature Combustion," *SAE Technical Papers*, SAE International, 2020.

10. A. Feuerstein, J. Knapp, T. Taylor, A. Ashary, A. Bolcavage, and N. Hitchman, Technical and Economical Aspects of Current Thermal Barrier Coating Systems for Gas Turbine Engines by Thermal Spray and EBPVD: A Review, *Journal of Thermal Spray Technology*, Springer Science and Business Media, LLC, 2008, **17**(2), p 199–213.

11. E. Bakan and R. Vaßen, Ceramic Top Coats of Plasma-Sprayed Thermal Barrier Coatings: Materials, Processes, and Properties, *Journal of Thermal Spray Technology*, Springer New York LLC, 2017, **26**(6), p 992–1010.

12. Huibin. Xu and Hongbo. Guo, "Thermal Barrier Coatings," Woodhead Pub Ltd, 2011.

13. G. Witz, M. Schaudinn, J. Sopka, and T. Buecklers, Development of Advanced Thermal Barrier Coatings With Improved Temperature Capability, *J Eng Gas Turbine Power*, American Society of Mechanical Engineers (ASME), 2017, **139**(8).

14. E. V. Dudnik, S.N. Lakiza, N.I. Hrechanyuk, A.K. Ruban, V.P. Red'ko, M.S. Hlabay, and A.B. Myloserdov, The Gd2Zr2O7-Based Materials for Thermal Barrier Coatings, *Powder Metallurgy and Metal Ceramics*, Springer New York LLC, 2018, **57**(5–6), p 301–315.

15. Vaßen R., F. Traeger, and D. Stöver, Materials with Pyrochlore Structures and High Melting Points Show Promising Thermophysical Properties. Espe-Cially Interesting Candidates Are La, *Int J Appl Ceram Technol*, Traeger, and Stöver, 2004, **1**(4), p 351–361, www.ceramics.org/ACT.

16. D. Zhou, D.E. Mack, E. Bakan, G. Mauer, D. Sebold, O. Guillon, and R. Vaßen, Thermal Cycling Performances of Multilayered Yttria-Stabilized Zirconia/Gadolinium Zirconate Thermal Barrier Coatings, *Journal of the American Ceramic Society*, Blackwell Publishing Inc., 2020, **103**(3), p 2048–2061.

17. S. Sampath, U. Schulz, M.O. Jarligo, and S. Kuroda, Processing Science of Advanced Thermal-Barrier Systems, *MRS Bull*, 2012, **37**(10), p 903–910.

18. C.M. Rost, E. Sachet, T. Borman, A. Moballegh, E.C. Dickey, D. Hou, J.L. Jones, S. Curtarolo, and J.P. Maria, Entropy-Stabilized Oxides, *Nat Commun*, Nature Publishing Group, 2015, **6**, p 8485.

19. K. Chen, X. Pei, L. Tang, H. Cheng, Z. Li, C. Li, X. Zhang, and L. An, A Five-Component Entropy-Stabilized Fluorite Oxide, *J Eur Ceram Soc*, Elsevier Ltd, 2018, **38**(11), p 4161–4164.

20. S. Akrami, P. Edalati, M. Fuji, and K. Edalati, "High-Entropy Ceramics: Review of Principles, Production and Applications," *Materials Science and Engineering R: Reports*, Elsevier Ltd, 2021, p 100644.

21. C. Oses, C. Toher, and S. Curtarolo, "High-Entropy Ceramics," *Nature Reviews Materials*, Nature Research, 2020, p 295–309.

22. J. Liu, G. Shao, D. Liu, K. Chen, K. Wang, B. Ma, K. Ren, and Y. Wang, Design and Synthesis of Chemically Complex Ceramics from the Perspective of Entropy, *Mater Today Adv*, Elsevier Ltd, 2020, **8**, p 100114.

23. K. Ren, Q. Wang, G. Shao, X. Zhao, and Y. Wang, Multicomponent High-Entropy Zirconates with Comprehensive Properties for Advanced Thermal Barrier Coating, *Scr Mater*, Acta Materialia Inc, 2020, **178**, p 382–386.

24. D. Beagle, B. Moran, M. Mcdufford, and M. Merine, "GER-3620P Heavy-Duty Gas Turbine Operating and Maintenance Considerations," 2021, https://www.ge.com/gas-power/resources/technical-downloads/ger-3620p-operation-maintenance-considerations. Accessed 24 November 2022.

25. N. Curry, N. Markocsan, X.H. Li, A. Tricoire, and M. Dorfman, "Next Generation Thermal Barrier Coatings for the Gas Turbine Industry," *Journal of Thermal Spray Technology*, 2011, p 108–115.

26. Z.-Y. Wei, G.-H. Meng, L. Chen, G.-R. Li, M.-J. Liu, W.-X. Zhang, L.-N. Zhao, Q. Zhang, X.-D. Zhang, C.-L. Wan, Z.-X. Qu, L. Chen, J. Feng, L. Liu, H. Dong, Z.-B. Bao, X.-F. Zhao, X.-F. Zhang,

L. Guo, L. Wang, B. Cheng, W.-W. Zhang, P.-Y. Xu, G.-J. Yang, H.-N. Cai, H. Cui, Y. Wang, F.-X. Ye, Z. Ma, W. Pan, et al., Progress in Ceramic Materials and Structure Design toward Advanced Thermal Barrier Coatings, *Journal of Advanced Ceramics*, 2022, **11**(7), p 985–1068, doi:10.1007/s40145-022-0581-7.

27. M.J. Donachie and S.J. Donachie, "Mechanical Engineers' Handbook: Materials and Mechanical Design - Chapter 8: 'SELECTION OF SUPERALLOYS FOR DESIGN,'" M. Kutz, Ed., 3rd ed., John Wiley & Sons, Inc., 2005.

28. C. Mercer, J.R. Williams, D.R. Clarke, and A.G. Evans, On a Ferroelastic Mechanism Governing the Toughness of Metastable Tetragonal-Prime (T′) Yttria-Stabilized Zirconia, *Proceedings of the Royal Society A: Mathematical, Physical and Engineering Sciences*, Royal Society, 2007, **463**(2081), p 1393–1408.

29. R.S. Lima, B.M.H. Guerreiro, and M. Aghasibeig, Microstructural Characterization and Room-Temperature Erosion Behavior of As-Deposited SPS, EB-PVD and APS YSZ-Based TBCs, *Journal of Thermal Spray Technology*, Springer New York LLC, 2019, **28**(1–2), p 223–232.

30. J.W.D. Callister and D.G. Rethwisch, "Materials Science and Engineering," Nineth, Wiley, 2013.

31. N.P. Padture, M. Gell, and E.H. Jordan, "Thermal Barrier Coatings for Gas-Turbine Engine Applications," *New Series*, 2002, p 280–284.

32. M. Parchovianský, I. Parchovianská, O. Hanzel, Z. Netriová, and A. Pakseresht, Phase Evaluation, Mechanical Properties and Thermal Behavior of Hot-Pressed LC-YSZ Composites for TBC Applications, *Materials*, MDPI, 2022, **15**(8).

33. G. Dwivedi, V. Viswanathan, S. Sampath, A. Shyam, and E. Lara-Curzio, Fracture Toughness of Plasma-Sprayed Thermal Barrier Ceramics: Influence of Processing, Microstructure, and Thermal Aging, *Journal of the American Ceramic Society*, 2014, **97**(9), p 2736–2744.

34. S. Mahade, C. Ruelle, N. Curry, J. Holmberg, S. Björklund, N. Markocsan, and P. Nylén, Understanding the Effect of Material Composition and Microstructural Design on the Erosion Behavior of Plasma Sprayed Thermal Barrier Coatings, *Appl Surf Sci*, Elsevier B.V., 2019, **488**, p 170–184.

35. A. Pakseresht, F. Sharifianjazi, A. Esmaeilkhanian, L. Bazli, M. Reisi Nafchi, M. Bazli, and K. Kirubaharan, "Failure Mechanisms and Structure Tailoring of YSZ and New Candidates for Thermal Barrier Coatings: A Systematic Review," *Materials and Design*, Elsevier Ltd, 2022.

36. B. Xiao, X. Huang, T. Robertson, Z. Tang, and R. Kearsey, Sintering Resistance of Suspension Plasma Sprayed 7YSZ TBC under Isothermal and Cyclic Oxidation, *J Eur Ceram Soc*, Elsevier Ltd, 2020, **40**(5), p 2030–2041.

37. A. Cipitria, I.O. Golosnoy, and T.W. Clyne, A Sintering Model for Plasma-Sprayed Zirconia Thermal Barrier Coatings. Part II: Coatings Bonded to a Rigid Substrate, *Acta Mater*, 2009, **57**(4), p 993–1003.

38. D.L. Poerschke, R.W. Jackson, and C.G. Levi, Silicate Deposit Degradation of Engineered Coatings in Gas Turbines: Progress Toward Models and Materials Solutions, *Annu Rev Mater Res*, 2017, **47**, p 297–330, doi:10.1146/annurev-matsci-010917.

39. X. Shan, L. Luo, W. Chen, Z. Zou, F. Guo, L. He, A. Zhang, X. Zhao, and P. Xiao, Pore Filling Behavior of YSZ under CMAS Attack: Implications for Designing Corrosion-Resistant Thermal Barrier Coatings, *Journal of the American Ceramic Society*, Blackwell Publishing Inc., 2018, **101**(12), p 5756–5770.

40. F.H. Stott, D.J. de Wet, and R. Taylor, Degradation of Thermal-Barrier Coatings at Very High Temperatures, *MRS Bull*, 1994, **19**(10), p 46–49, doi:10.1557/S0883769400048223.

41. A.G. Evans and J.W. Hutchinson, The Mechanics of Coating Delamination in Thermal Gradients, *Surf Coat Technol*, 2007, **201**(18), p 7905–7916.

42. R.S. Lima and B.R. Marple, Nanostructured YSZ Thermal Barrier Coatings Engineered to Counteract Sintering Effects, *Materials Science and Engineering A*, 2008, **485**(1–2), p 182–193.

43. X. Zhou, T. Chen, J. Yuan, Z. Deng, H. Zhang, J. Jiang, and X. Cao, Failure of Plasma Sprayed Nano-Zirconia-Based Thermal Barrier Coatings Exposed to Molten CaO–MgO–Al2O3–SiO2 Deposits, *Journal of the American Ceramic Society*, Blackwell Publishing Inc., 2019, **102**(10), p 6357–6371.

44. P.M. Kelly and C.J. Wauchope, The Tetragonal to Monoclinic Martensitic Transformation in Zirconia, *Key Eng Mater*, Trans Tech Publications Ltd, 1998, **153–154**, p 97–124, doi:10.4028/www.scientific.net/KEM.153-154.97.

45. D.M. Lipkin, J.A. Krogstad, Y. Gao, C.A. Johnson, W.A. Nelson, and C.G. Levi, Phase Evolution upon Aging of Air-Plasma Sprayed T′-Zirconia Coatings: I - Synchrotron X-Ray Diffraction, *Journal of the American Ceramic Society*, 2013, **96**(1), p 290–298.

46. A. Rabiei and A.G. Evans, Failure Mechanisms Associated with The Thermally Grown Oxide In Plasma-Sprayed Thermal Barrier Coatings, *Acta mater*, 2000, **48**, p 3963–3976, www.elsevier.com/locate/actamat.

47. Dutton, R, R. Wheeler, K.S. Ravichandran, and K. An, Effect of Heat Treatment on the Thermal Conductivity of Plasma-Sprayed Thermal Barrier Coatings, *Journal of Thermal Spray Technology*, 2000, **9**, p 204–209.

48. R. Bjørk, H.L. Frandsen, and N. Pryds, Modeling the Microstructural Evolution during Constrained Sintering, *Journal of the American Ceramic Society*, Blackwell Publishing Inc., 2015, **98**(11), p 3490–3495.

49. S. Taub and J. Kim, “Constrained Sintering Stress -Review,” *EKC 2009 Proceedings of EU-Korea Conference on Science and Technology*, Springer Proceedings in Physics 135, 2008, p 163–173, http://www.springer.com/series/361/.

50. M.A. Subramanian, G. Aravamudan, and G.V.S. Rao, Oxide Pyrochlores A Review, *Prog. Solid State Chem*, 1983, **15**, p 55–143.

51. H. Junjie, H. Guo, L. Jing, and T. Jingchao, New Class of High-Entropy Defect Fluorite Oxides RE2(Ce0.2Zr0.2Hf0.2Sn0.2Ti0.2)2O7 (RE = Y, Ho, Er, or Yb) as Promising Thermal Barrier Coatings, *J Eur Ceram Soc*, Elsevier Ltd, 2021, **41**(12), p 6080–6086.

52. J. Shi, Z. Qu, and Q. Wang, “Influence of Temperature on the Order-Disorder Transition in Gd2Zr2O7,” *Key Engineering Materials*, Trans Tech Publications Ltd, 2016, p 386–389.

53. J. Zhang, X. Guo, Y.G. Jung, L. Li, and J. Knapp, Lanthanum Zirconate Based Thermal Barrier Coatings: A Review, *Surf Coat Technol*, Elsevier B.V., 2017, **323**, p 18–29.

54. Q. Xu, W. Pan, J. Wang, C. Wan, L. Qi, H. Miao, K. Mori, and T. Torigoe, “Rare-Earth Zirconate Ceramics with Fluorite Structure for Thermal Barrier Coatings,” *Journal of the American Ceramic Society*, 2006, p 340–342.

55. Y. Ozgurluk, K.M. Doleker, and A.C. Karaoglanli, Hot Corrosion Behavior of YSZ, Gd2Zr2O7, and YSZ/Gd2Zr2O7 Thermal Barrier Coatings Exposed to Molten Sulfate and Vanadate Salt, *Appl Surf Sci*, Elsevier B.V., 2018, **438**, p 96–113.

56. H. Khan, Y. Iqbal, M. Khan, and Y. Zeng, Variations in the Thermal Conductivity of La2Zr2O7 and Gd2Zr2O7 with Variable La/Gd Concentrations, *Physica B*, Elsevier B.V., 2021, **614**.

57. R. Vassen, X. Cao, F. Tietz, D. Basu, and D. Stöver, Zirconates as New Materials for Thermal Barrier Coatings, *Journal of the American Ceramic Society*, American Ceramic Soc, 2000, **83**(8), p 2023–2028.

58. G. Moskal, L. Swadźba, M. Hetmańczyk, B. Witala, B. Mendala, J. Mendala, and P. Sosnowy, Characterisation of the Microstructure and Thermal Properties of Nd 2Zr 2O 7 and Nd 2Zr 2O 7/YSZ Thermal Barrier Coatings, *J Eur Ceram Soc*, 2012, **32**(9), p 2035–2042.

59. D. Migas, G. Moskal, and S. Jucha, Hot Corrosion Behavior of Double-Phase Nd2Zr2O7-YSZ Thermal Barrier Coatings, *Surf Coat Technol*, Elsevier B.V., 2022, **449**.

60. K.M. Doleker, A.C. Karaoglanli, Y. Ozgurluk, and A. Kobayashi, Performance of Single YSZ, Gd2Zr2O7 and Double-Layered YSZ/Gd2Zr2O7 Thermal Barrier Coatings in Isothermal Oxidation Test Conditions, *Vacuum*, Elsevier Ltd, 2020, **177**.

61. G. Moskal, A. Jasik, M. Mikuśkiewicz, and S. Jucha, Thermal Resistance Determination of Sm2Zr2O7 + 8YSZ Composite Type of TBC, *Appl Surf Sci*, Elsevier B.V., 2020, **515**.

62. H.X. Wu, Z. Ma, L. Liu, Y.B. Liu, and D.Y. Wang, Thermal Cycling Behavior and Bonding Strength of Single-Ceramic-Layer Sm2Zr2O7 and Double-Ceramic-Layer Sm2Zr2O7/8YSZ Thermal Barrier Coatings Deposited by Atmospheric Plasma Spraying, *Ceram Int*, Elsevier Ltd, 2016, **42**(11), p 12922–12927.

63. J.W. Fergus, Zirconia and Pyrochlore Oxides for Thermal Barrier Coatings in Gas Turbine Engines, *Metallurgical and Materials Transactions E*, Springer Science and Business Media LLC, 2014, **1**(2), p 118–131.

64. J. Wu, X. Wei, N.P. Padture, P.G. Klemens, M. Gell, E. García, P. Miranzo, and M.I. Osendi, Low-Thermal-Conductivity Rare-Earth Zirconates for Potential Thermal-Barrier-Coating Applications, *Journal of the American Ceramic Society*, American Ceramic Society, 2002, **85**(12), p 3031–3035.

65. H. Wang, E. Tarwater, X. Zhang, Z. Sheng, and J.W. Fergus, "PYROCHLORE LANTHANIDE ZIRCONATES FOR THERMAL BARRIER COATINGS," n.d., http://ebookcentral.proquest.com/lib/ubishops/detail.action?docID=4206460.

66. R. Vaßen, F. Traeger, and D. Stöver, New Thermal Barrier Coatings Based on Pyrochlore/YSZ Double-Layer Systems, *Int J Appl Ceram Technol*, Traeger, and Stöver, 2004, **1**(4), p 352, www.ceramics.org/ACT.

67. M.A. Helminiak, N.M. Yanar, F.S. Pettit, T.A. Taylor, and G.H. Meier, Factors Affecting the Microstructural Stability and Durability of Thermal Barrier Coatings Fabricated by Air Plasma Spraying, *Materials and Corrosion*, John Wiley & Sons, Ltd, 2012, **63**(10), p 929–939, doi:https://doi.org/10.1002/maco.201206646.

68. G. Dwivedi, V. Viswanathan, S. Sampath, A. Shyam, and E. Lara-Curzio, Fracture Toughness of Plasma-Sprayed Thermal Barrier Ceramics: Influence of Processing, Microstructure, and Thermal Aging, *Journal of the American Ceramic Society*, 2014, **97**(9), p 2736–2744.

69. R.M. Leckie, S. Krämer, M. Rühle, and C.G. Levi, Thermochemical Compatibility between Alumina and ZrO2-GdO 3/2 Thermal Barrier Coatings, *Acta Mater*, 2005, **53**(11), p 3281–3292.

70. S. Mahade, N. Curry, S. Björklund, N. Markocsan, and S. Joshi, Durability of Gadolinium Zirconate/YSZ Double-Layered Thermal Barrier Coatings under Different Thermal Cyclic Test Conditions, *Materials*, MDPI AG, 2019, **12**(14).

71. W. Ma, D. Mack, J. Malzbender, R. Vaßen, and D. Stöver, Yb2O3 and Gd2O3 Doped Strontium Zirconate for Thermal Barrier Coatings, *J Eur Ceram Soc*, 2008, **28**(16), p 3071–3081.

72. R. Vaßen, G. Pracht, and D. Stöver, New Thermal Barrier Coating Systems with a Graded Ceramic Coating, *Proc. of the International Thermal Spray Conference*, 2002, p 202–207.

73. H. Chen, Y. Liu, Y. Gao, S. Tao, and H. Luo, Design, Preparation, and Characterization of Graded YSZ/La 2Zr2O7 Thermal Barrier Coatings, *Journal of the American Ceramic Society*, 2010, **93**(6), p 1732–1740.

74. B.S. Murty, J.W. Yeh, and S. Ranganathan, "High-Entropy Alloys," Butterworth-Heinemann, 2014.

75. J.W. Yeh, Alloy Design Strategies and Future Trends in High-Entropy Alloys, *JOM*, 2013, **65**(12), p 1759–1771.

76. J.W. Yeh and S.J. Lin, Breakthrough Applications of High-Entropy Materials, *J Mater Res*, Cambridge University Press, 2018, **33**(19), p 3129–3137.

77. G.R. Lumpkin, M. Pruneda, S. Rios, K.L. Smith, K. Trachenko, K.R. Whittle, and N.J. Zaluzec, Nature of the Chemical Bond and Prediction of Radiation Tolerance in Pyrochlore and Defect Fluorite Compounds, *J Solid State Chem*, 2007, **180**(4), p 1512–1518, doi:https://doi.org/10.1016/j.jssc.2007.01.028.

78. H. Shahbazi, H. Vakilifrd, R.B. Nair, A.C. Liberati, R.S. Lima, and C. Moreau, "High Entropy Alloy (HEA) Bond Coats for Thermal Barrier Coatings (TBCs)—A Review," *Thermal Spray Proceedings, ITSC 2023*, 2023, doi:https://doi.org/10.31399/asm.cp.itsc2023p0659.

79. H. Xiang, Y. Xing, F. zhi Dai, H. Wang, L. Su, L. Miao, G. Zhang, Y. Wang, X. Qi, L. Yao, H. Wang, B. Zhao, J. Li, and Y. Zhou, High-Entropy Ceramics: Present Status, Challenges, and a Look Forward, *Journal of Advanced Ceramics*, Tsinghua University, 2021, **10**(3), p 385–441.

80. A.J. Wright and J. Luo, A Step Forward from High-Entropy Ceramics to Compositionally Complex Ceramics: A New Perspective, *J Mater Sci*, Springer, 2020, **55**(23), p 9812–9827.

81. A. Sarkar, B. Breitung, and H. Hahn, High Entropy Oxides: The Role of Entropy, Enthalpy and Synergy, *Scr Mater*, Acta Materialia Inc, 2020, **187**, p 43–48.

82. D. Bérardan, S. Franger, D. Dragoe, A.K. Meena, and N. Dragoe, Colossal Dielectric Constant in High Entropy Oxides, *physica status solidi (RRL)–Rapid Research Letters*, Wiley Online Library, 2016, **10**(4), p 328–333.

83. Z. Zhao, H. Chen, H. Xiang, F.Z. Dai, X. Wang, W. Xu, K. Sun, Z. Peng, and Y. Zhou, (Y0.25Yb0.25Er0.25Lu0.25)2(Zr0.5Hf0.5)2O7: A Defective Fluorite Structured High Entropy

Ceramic with Low Thermal Conductivity and Close Thermal Expansion Coefficient to Al2O3, *J Material Science and Technology*, Chinese Society of Metals, 2020, **39**, p 167–172.

84. L. Xu, H. Wang, L. Su, D. Lu, K. Peng, and H. Gao, A New Class of High-Entropy Fluorite Oxides with Tunable Expansion Coefficients, Low Thermal Conductivity and Exceptional Sintering Resistance, *J Eur Ceram Soc*, Elsevier Ltd, 2021, **41**(13), p 6670–6676.

85. L. Spiridigliozzi, C. Ferone, R. Cioffi, and G. Dell'Agli, A Simple and Effective Predictor to Design Novel Fluorite-Structured High Entropy Oxides (HEOs), *Acta Mater*, Acta Materialia Inc, 2021, **202**, p 181–189.

86. J. Gild, M. Samiee, J.L. Braun, T. Harrington, H. Vega, P.E. Hopkins, K. Vecchio, and J. Luo, High-Entropy Fluorite Oxides, *J Eur Ceram Soc*, Elsevier Ltd, 2018, **38**(10), p 3578–3584.

87. Y. Yang, H. Li, B. Duan, Q. Feng, C. Li, X. Lu, G. Chen, and C. Li, A Novel High Entropy Perovskite Oxide with Co-Substitution in A and B Sites (Ca1/3Sr1/3Ba1/3)(Y1/4Zr1/2Nb1/4)O3 Design, Synthesis and Structural Characterization, *Ceram Int*, Elsevier BV, 2022.

88. S. Jiang, T. Hu, J. Gild, N. Zhou, J. Nie, M. Qin, T. Harrington, K. Vecchio, and J. Luo, A New Class of High-Entropy Perovskite Oxides, *Scr Mater*, Acta Materialia Inc, 2018, **142**, p 116–120.

89. Z. Teng, L. Zhu, Y. Tan, S. Zeng, Y. Xia, Y. Wang, and H. Zhang, Synthesis and Structures of High-Entropy Pyrochlore Oxides, *J Eur Ceram Soc*, Elsevier Ltd, 2020, **40**(4), p 1639–1643.

90. H. Liu, S. Pang, C. Liu, Y. Wu, and G. Zhang, High-entropy Yttrium Pyrochlore Ceramics with Glass-like Thermal Conductivity for Thermal Barrier Coating Application, *Journal of the American Ceramic Society*, 2022, **105**(10), p 6437–6448, doi:10.1111/jace.18588.

91. D. Guo, F. Zhou, B. Xu, Y. Wang, and Y. Wang, Synthesis and Characterization of High-Entropy (La0.2Nd0.2Sm0.2Gd0.2Yb0.2)2(Zr0.75Ce0.25)2O7 Nanopowders, *Ceram Int*, 2022, **48**(21), p 32532–32535, doi:10.1016/j.ceramint.2022.07.207.

92. Z. Teng, Y. Tan, S. Zeng, Y. Meng, C. Chen, X. Han, and H. Zhang, Preparation and Phase Evolution of High-Entropy Oxides A2B2O7 with Multiple Elements at A and B Sites, *J Eur Ceram Soc*, Elsevier Ltd, 2021, **41**(6), p 3614–3620.

93. F. Li, L. Zhou, J.X. Liu, Y. Liang, and G.J. Zhang, High-Entropy Pyrochlores with Low Thermal Conductivity for Thermal Barrier Coating Materials, *Journal of Advanced Ceramics*, Tsinghua University, 2019, **8**(4), p 576–582.

94. D.A. Vinnik, E.A. Trofimov, V.E. Zhivulin, O. V Zaitseva, S.A. Gudkova, A.Yu. Starikov, D.A. Zherebtsov, A.A. Kirsanova, M. Häßner, and R. Niewa, High-Entropy Oxide Phases with Magnetoplumbite Structure, *Ceram Int*, 2019, **45**(10), p 12942–12948, doi:https://doi.org/10.1016/j.ceramint.2019.03.221.

95. C. Zhao, F. Ding, Y. Lu, L. Chen, and Y.-S. Hu, High-Entropy Layered Oxide Cathodes for Sodium-Ion Batteries, *Angewandte Chemie International Edition*, John Wiley & Sons, Ltd, 2020, **59**(1), p 264–269, doi:https://doi.org/10.1002/anie.201912171.

96. B. Musicó, Q. Wright, T.Z. Ward, A. Grutter, E. Arenholz, D. Gilbert, D. Mandrus, and V. Keppens, Tunable Magnetic Ordering through Cation Selection in Entropic Spinel Oxides, *Phys Rev Mater*, 2019, **3**(10), doi:10.1103/PhysRevMaterials.3.104416.

97. J. Dąbrowa, M. Stygar, A. Mikuła, A. Knapik, K. Mroczka, W. Tejchman, M. Danielewski, and M. Martin, Synthesis and Microstructure of the (Co,Cr,Fe,Mn,Ni)3O4 High Entropy Oxide Characterized by Spinel Structure, *Mater Lett*, 2018, **216**, p 32–36, doi:https://doi.org/10.1016/j.matlet.2017.12.148.

98. T. Parida, A. Karati, K. Guruvidyathri, B.S. Murty, and G. Markandeyulu, Novel Rare-Earth and Transition Metal-Based Entropy Stabilized Oxides with Spinel Structure, *Scr Mater*, Elsevier, 2020, **178**, p 513–517.

99. H. Chen, W. Lin, Z. Zhang, K. Jie, D.R. Mullins, X. Sang, S.-Z. Yang, C.J. Jafta, C.A. Bridges, X. Hu, R.R. Unocic, J. Fu, P. Zhang, and S. Dai, Mechanochemical Synthesis of High Entropy Oxide Materials under Ambient Conditions: Dispersion of Catalysts via Entropy Maximization, *ACS Mater Lett*, 2019, **1**(1), p 83–88, doi:10.1021/acsmaterialslett.9b00064.

100. D. Zhang, Y. Yu, X. Feng, Z. Tian, and R. Song, Thermal Barrier Coatings with High-Entropy Oxide as a Top Coat, *Ceram Int*, Elsevier Ltd, 2022, **48**(1), p 1349–1359.

101. Y.F. Ye, Q. Wang, J. Lu, C.T. Liu, and Y. Yang, "High-Entropy Alloy: Challenges and Prospects," *Materials Today*, Elsevier B.V., 2016, p 349–362.

102. G. Anand, A.P. Wynn, C.M. Handley, and C.L. Freeman, Phase Stability and Distortion in High-Entropy Oxides, *Acta Mater*, Acta Materialia Inc, 2018, **146**, p 119–125.

103. Y.P. Wang, G.Y. Gan, W. Wang, Y. Yang, and B.Y. Tang, Ab Initio Prediction of Mechanical and Electronic Properties of Ultrahigh Temperature High-Entropy Ceramics (Hf0.2Zr0.2Ta0.2M0.2Ti0.2)B2 (M = Nb, Mo, Cr), *Phys Status Solidi B Basic Res*, Wiley-VCH Verlag, 2018, **255**(8).

104. T. Wen, B. Ye, H. Liu, S. Ning, C.Z. Wang, and Y. Chu, Formation Criterion for Binary Metal Diboride Solid Solutions Established through Combinatorial Methods, *Journal of the American Ceramic Society*, Blackwell Publishing Inc., 2020, **103**(5), p 3338–3348.

105. Y. Yang, W. Wang, G.Y. Gan, X.F. Shi, and B.Y. Tang, Structural, Mechanical and Electronic Properties of (TaNbHfTiZr)C High Entropy Carbide under Pressure: Ab Initio Investigation, *Physica B Condens Matter*, Elsevier B.V., 2018, **550**, p 163–170.

106. D. Liu, T. Wen, B. Ye, and Y. Chu, Synthesis of Superfine High-Entropy Metal Diboride Powders, *Scr Mater*, Acta Materialia Inc, 2019, **167**, p 110–114.

107. T. Wen, H. Liu, B. Ye, D. Liu, and Y. Chu, High-Entropy Alumino-Silicides: A Novel Class of High-Entropy Ceramics, *Sci China Mater*, Science China Press, 2020, **63**(2), p 300–306.

108. B. Ye, T. Wen, M.C. Nguyen, L. Hao, C.Z. Wang, and Y. Chu, First-Principles Study, Fabrication and Characterization of (Zr 0.25 Nb 0.25 Ti 0.25 V 0.25)C High-Entropy Ceramics, *Acta Mater*, Acta Materialia Inc, 2019, **170**, p 15–23.

109. H. Yang, G. Lin, H. Bu, H. Liu, L. Yang, W. Wang, X. Lin, C. Fu, Y. Wang, and C. Zeng, Single-Phase Forming Ability of High-Entropy Ceramics from a Size Disorder Perspective: A Case Study of (La0.2Eu0.2Gd0.2Y0.2Yb0.2)2Zr2O7, *Ceram Int*, Elsevier Ltd, 2022, **48**(5), p 6956–6965.

110. Q.F. He, Z.Y. Ding, Y.F. Ye, and Y. Yang, "Design of High-Entropy Alloy: A Perspective from Nonideal Mixing," *JOM*, Minerals, Metals and Materials Society, 2017, p 2092–2098.

111. X. Yang and Y. Zhang, Prediction of High-Entropy Stabilized Solid-Solution in Multi-Component Alloys, *Mater Chem Phys*, Elsevier Ltd, 2012, **132**(2–3), p 233–238.

112. Y. Zhang, T.T. Zuo, Z. Tang, M.C. Gao, K.A. Dahmen, P.K. Liaw, and Z.P. Lu, "Microstructures and Properties of High-Entropy Alloys," *Progress in Materials Science*, Elsevier Ltd, 2014, p 1–93.

113. P. Hutterer and M. Lepple, Influence of Composition on Structural Evolution of High-Entropy Zirconates—Cationic Radius Ratio and Atomic Size Difference, *Journal of the American Ceramic Society*, John Wiley and Sons Inc, 2022.

114. P. Sarker, T. Harrington, C. Toher, C. Oses, M. Samiee, J.P. Maria, D.W. Brenner, K.S. Vecchio, and S. Curtarolo, High-Entropy High-Hardness Metal Carbides Discovered by Entropy Descriptors, *Nat Commun*, Nature Publishing Group, 2018, **9**(1).

115. K.C. Pitike, A. Macias, M. Eisenbach, C.A. Bridges, and V.R. Cooper, Computationally Accelerated Discovery of High Entropy Pyrochlore Oxides, *Chemistry of Materials*, American Chemical Society, 2022, **34**(4), p 1459–1472.

116. M.C. Gao, D.B. Miracle, D. Maurice, X. Yan, Y. Zhang, and J.A. Hawk, High-Entropy Functional Materials, *J Mater Res*, Cambridge University Press, 2018, **33**(19), p 3138–3155.

117. M.C. Gao, C. Zhang, P. Gao, F. Zhang, L.Z. Ouyang, M. Widom, and J.A. Hawk, Thermodynamics of Concentrated Solid Solution Alloys, *Curr Opin Solid State Mater Sci*, Elsevier Ltd, 2017, **21**(5), p 238–251.

118. R.Z. Zhang and M.J. Reece, "Review of High Entropy Ceramics: Design, Synthesis, Structure and Properties," *Journal of Materials Chemistry A*, Royal Society of Chemistry, 2019, p 22148–22162.

119. S.L. Liew, X.P. Ni, F. Wei, S.Y. Tan, M.T. Luai, P.C. Lim, S.L. Teo, N.B.M. Rafiq, J. Zhou, and S. Wang, High-Entropy Fluorite Oxides: Atomic Stabiliser Effects on Thermal-Mechanical Properties, *J Eur Ceram Soc*, 2022, **42**(14), p 6608–6613, doi:https://doi.org/10.1016/j.jeurceramsoc.2022.07.026.

120. M. Du, S. Liu, Y. Ge, Z. Li, T. Wei, X. Yang, and J. Dong, Preparation and Effect of Grain Size on the Thermal Stability, Phase Transition, Mechanical Property, and Photocatalytic Property of Pyrochlore (La0.2Nd0.2Sm0.2Gd0.2Y0.2)2Zr2O7 High-Entropy Oxide, *Ceram Int*, 2022, **48**(14), p 20667–20674, doi:https://doi.org/10.1016/j.ceramint.2022.04.046.

121. D. Berardan, A.K. Meena, S. Franger, C. Herrero, and N. Dragoe, Controlled Jahn-Teller Distortion in (MgCoNiCuZn)O-Based High Entropy Oxides, *J Alloys Compd*, 2017, **704**, p 693–700, doi:https://doi.org/10.1016/j.jallcom.2017.02.070.

122. A. Sarkar, L. Velasco, D. Wang, Q. Wang, G. Talasila, L. de Biasi, C. Kübel, T. Brezesinski, S.S. Bhattacharya, H. Hahn, and B. Breitung, High Entropy Oxides for Reversible Energy Storage, *Nat Commun*, 2018, **9**(1), doi:10.1038/s41467-018-05774-5.

123. Y. Guo, S. Feng, J. Fu, Y. Yang, R. Zheng, H. Wang, and J. Li, Multi-Component Oxide Lens Glass with Ultra-High Mechanical Properties Inspired by the High-Entropy Concept, *Ceram Int*, 2022, doi:https://doi.org/10.1016/j.ceramint.2022.11.096.

124. J. Zhang, J. Yan, S. Calder, Q. Zheng, M.A. McGuire, D.L. Abernathy, Y. Ren, S.H. Lapidus, K. Page, H. Zheng, J.W. Freeland, J.D. Budai, and R.P. Hermann, Long-Range Antiferromagnetic Order in a Rocksalt High Entropy Oxide, *Chemistry of Materials*, American Chemical Society, 2019, **31**(10), p 3705–3711, doi:10.1021/acs.chemmater.9b00624.

125. R. Witte, A. Sarkar, L. Velasco, R. Kruk, R.A. Brand, B. Eggert, K. Ollefs, E. Weschke, H. Wende, and H. Hahn, Magnetic Properties of Rare-Earth and Transition Metal Based Perovskite Type High Entropy Oxides, *J Appl Phys*, AIP Publishing LLC, 2020, **127**(18), p 185109.

126. D. Song, T. Song, U. Paik, G. Lyu, Y.G. Jung, H.B. Jeon, and Y.S. Oh, Glass-like Thermal Conductivity in Mass-Disordered High-Entropy (Y,Yb)2(Ti, Zr, Hf)2O7 for Thermal Barrier Material, *Mater Des*, Elsevier Ltd, 2021, **210**.

127. M.-H. Chuang, M.-H. Tsai, W.-R. Wang, S.-J. Lin, and J.-W. Yeh, Microstructure and Wear Behavior of AlxCo1. 5CrFeNi1. 5Tiy High-Entropy Alloys, *Acta Mater*, Elsevier, 2011, **59**(16), p 6308–6317.

128. Z. Zhao, H. Xiang, F.Z. Dai, Z. Peng, and Y. Zhou, (La0.2Ce0.2Nd0.2Sm0.2Eu0.2)2Zr2O: A Novel High-Entropy Ceramic with Low Thermal Conductivity and Sluggish Grain Growth Rate, *J Mater Sci Technol*, Chinese Society of Metals, 2019, **35**(11), p 2647–2651.

129. L. Zhou, F. Li, J.X. Liu, Q. Hu, W. Bao, Y. Wu, X. Cao, F. Xu, and G.J. Zhang, High-Entropy Thermal Barrier Coating of Rare-Earth Zirconate: A Case Study on (La0.2Nd0.2Sm0.2Eu0.2Gd0.2)2Zr2O7 Prepared by Atmospheric Plasma Spraying, *J Eur Ceram Soc*, Elsevier Ltd, 2020, **40**(15), p 5731–5739.

130. N.J. Hess, B.D. Begg, S.D. Conradson, D.E. McCready, P.L. Gassman, and W.J. Weber, Spectroscopic Investigations of the Structural Phase Transition in Gd2(Ti1-YZry)2O7 Pyrochlores, *Journal of Physical Chemistry B*, 2002, **106**(18), p 4663–4677.

131. F. Qun-bo, Z. Feng, W. Fu-chi, and W. Lu, Molecular Dynamics Calculation of Thermal Expansion Coefficient of a Series of Rare-Earth Zirconates, *Comput Mater Sci*, 2009, **46**(3), p 716–719.

132. P.K. Schelling, S.R. Phillpot, and R.W. Grimes, Optimum Pyrochlore Compositions for Low Thermal Conductivity, *Philos Mag Lett*, 2004, **84**(2), p 127–137.

133. K.M. Doleker, Y. Ozgurluk, and A.C. Karaoglanli, TGO Growth and Kinetic Study of Single and Double Layered TBC Systems, *Surf Coat Technol*, Elsevier B.V., 2021, **415**, p 127–135.

134. S.M. Lakiza, V.P. Red'ko, and L.M. Lopato, Physicochemical Materials Research the Al2O3-ZrO2-Yb2O3 Phase Diagram. I. Isothermal Sections at 1250 And 1650°C, *Powder Metallurgy and Metal Ceramics*, 2008, **47**(4), p 60–69.

135. R.M. Leckie, S. Krämer, M. Rühle, and C.G. Levi, Thermochemical Compatibility between Alumina and ZrO2-GdO 3/2 Thermal Barrier Coatings, *Acta Mater*, 2005, **53**(11), p 3281–3292.

136. J. Sun, L. Guo, Y. Zhang, Y. Wang, K. Fan, and Y. Tang, Superior Phase Stability of High Entropy Oxide Ceramic in a Wide Temperature Range, *J Eur Ceram Soc*, Elsevier Ltd, 2022, **42**(12), p 5053–5064.

137. A.J. Wright, Q. Wang, C. Huang, A. Nieto, R. Chen, and J. Luo, From High-Entropy Ceramics to Compositionally-Complex Ceramics: A Case Study of Fluorite Oxides, *J Eur Ceram Soc*, Elsevier Ltd, 2020, **40**(5), p 2120–2129.

138. D. Song, M. Ryu, J. Pyeon, H.-B. Jeon, T. Song, U. Paik, B. Yang, Y.-G. Jung, and Y.-S. Oh, Phase-Reassembled High-Entropy Fluorites for Advanced Thermal Barrier Materials, *Journal of Materials Research and Technology*, Elsevier BV, 2023, **23**, p 2740–2749.

139. X. Luo, L. Luo, X. Zhao, H. Cai, S. Duan, C. Xu, S. Huang, H. Jin, and S. Hou, Single-Phase Rare-Earth High-Entropy Zirconates with Superior Thermal and Mechanical Properties, *J Eur Ceram Soc*, Elsevier Ltd, 2022, **42**(5), p 2391–2399.

140. T.Z. Tu, J.X. Liu, L. Zhou, Y. Liang, and G.J. Zhang, Graceful Behavior during CMAS Corrosion of a High-Entropy Rare-Earth Zirconate for Thermal Barrier Coating Material, *J Eur Ceram Soc*, Elsevier Ltd, 2022, **42**(2), p 649–657.

141. Y. Sun, H.-R. Mao, and P. Shen, Inhibition of Hotspot Formation by Alumina Addition in Flash Sintering of (La0.2Nd0.2Sm0.2Eu0.2Gd0.2)2Zr2O7 High-Entropy Ceramic, *J Eur Ceram Soc*, 2022, doi:10.1016/j.jeurceramsoc.2022.08.015.

142. Z.G. Liu, J.H. Ouyang, K.N. Sun, Y. Zhou, and J. Xiang, Preparation, Structure and Electrical Conductivity of Pyrochlore-Type Gd1-XEu2xSm1-XZr2O7 Ceramics with a Constant Lattice Parameter, *Electrochim Acta*, 2011, **56**(20), p 7045–7050.

143. X. Luo, R. Huang, C. Xu, S. Huang, S. Hou, and H. Jin, Designing High-Entropy Rare-Earth Zirconates with Tunable Thermophysical Properties for Thermal Barrier Coatings, *J Alloys Compd*, 2022, p 166714, doi:10.1016/j.jallcom.2022.166714.

144. M. Ma, Y. Han, Z. Zhao, J. Feng, and Y. Chu, Ultrafine-Grained High-Entropy Zirconates with Superior Mechanical and Thermal Properties, *J Mat*, 2022, doi:10.1016/j.jmat.2022.09.014.

145. D. Liu, S. Zhang, and Z. Wu, Lattice Energy Estimation for Inorganic Ionic Crystals, *Inorg Chem*, American Chemical Society, 2003, **42**(7), p 2465–2469, doi:10.1021/ic025902a.

146. L. Glasser, Lattice Energies of Crystals with Multiple Ions: A Generalized Kapustinskii Equation, *Inorg Chem*, American Chemical Society, 1995, **34**(20), p 4935–4936, doi:10.1021/ic00124a003.

147. A.F. Kapustinskii, Lattice Energy of Ionic Crystals, *Quarterly Reviews, Chemical Society*, 1956, **75**(4), p 455–658.

148. K.V.G. Kutty, S. Rajagopalan, C.K. Mathews, and U. V Varadaraju, Thermal Expansion Behaviour of Some Rare Earth Oxide Pyrochlores, *Mater Res Bull*, Elsevier, 1994, **29**(7), p 759–766.

149. J. Pannetier, "Energie Electrostatique Des Reseaux Pyrochlore," *Phys. Chem. Solids*, Pergamon Press, 1973.

150. R.L. Matcha, Theory of the Chemical Bond. 6 Accurate Relationship between Bond Energies and Electronegativity Differences, *J Am Chem Soc*, American Chemical Society, 1983, **105**(15), p 4859–4862, doi:10.1021/ja00353a002.

151. S. Deng, G. He, Z. Yang, J. Wang, J. Li, and L. Jiang, Calcium-Magnesium-Alumina-Silicate (CMAS) Resistant High Entropy Ceramic (Y0.2Gd0.2Er0.2Yb0.2Lu0.2)2Zr2O7 for Thermal Barrier Coatings, *J Mater Sci Technol*, Chinese Society of Metals, 2022, **107**, p 259–265.

152. R. Yan, W. Liang, Q. Miao, H. Zhao, R. Liu, J. Li, K. Zang, M. Dong, X. He, X. Gao, and Y. Song, Mechanical, Thermal and CMAS Resistance Properties of High-Entropy (Gd0.2Y0.2Er0.2Tm0.2Yb0.2)2Zr2O7 Ceramics, *Ceram Int*, Elsevier Ltd, 2023.

153. X. Luo, S. Huang, R. Huang, C. Xu, S. Hou, and H. Jin, Highly Anti-Sintering and Toughened Pyrochlore (Dy0.2Nd0.2Sm0.2Eu0.2Yb0.2)2Zr2O7 High-Entropy Ceramic for Advanced Thermal Barrier Coatings, *Ceram Int*, Elsevier Ltd, 2023.

154. X. Cao, R. Vassen, W. Fischer, F. Tietz, W. Jungen, and D. Stöver, Lanthanum-Cerium Oxide as a Thermal Barrier-Coating Material for High-Temperature Applications, *Advanced Materials*, 2003, **15**(17), p 1438–1442.

155. S.Y. Park, J.H. Kim, M.C. Kim, H.S. Song, and C.G. Park, Microscopic Observation of Degradation Behavior in Yttria and Ceria Stabilized Zirconia Thermal Barrier Coatings under Hot Corrosion, *Surf Coat Technol*, 2005, **190**(2), p 357–365, doi:https://doi.org/10.1016/j.surfcoat.2004.04.065.

156. W.B. Gong, C.K. Sha, D.Q. Sun, and W.Q. Wang, Microstructures and Thermal Insulation Capability of Plasma-Sprayed Nanostructured Ceria Stabilized Zirconia Coatings, *Surf Coat Technol*, 2006, **201**(6), p 3109–3115, doi:https://doi.org/10.1016/j.surfcoat.2006.06.041.

157. D. Jingmin, L. Kui, S. Weiwei, C. Xiaoge, L. Mengwei, X. Chuanyue, W. Zhuang, L. Xinchun, W. Bin, and Z. Hongsong, Influence of Ta2O5 Addition on Thermophysical Performance of Sm2Ce2O7, *J Mater Eng Perform*, Springer, 2021, **30**(8), p 5947–5952.

158. H. Dai, X. Zhong, J. Li, J. Meng, and X. Cao, Neodymium–Cerium Oxide as New Thermal Barrier Coating Material, *Surf Coat Technol*, 2006, **201**(6), p 2527–2533, doi:https://doi.org/10.1016/j.surfcoat.2006.04.016.

159. A. Tang, B. Li, W. Sang, Z. Hongsong, X. Chen, H. Zhang, and B. Ren, Thermophysical Performances of High-Entropy (La0.2Nd0.2Yb0.2Y0.2Sm0.2)2Ce2O7 and (La0.2Nd0.2Yb0.2Y0.2Lu0.2)2Ce2O7 Oxides, *Ceram Int*, Elsevier Ltd, 2022, **48**(4), p 5574–5580.

160. L. Lilin, L. Bin, S. Weiwei, Z. Hongsong, Z. Haoming, C. Xiaoge, and T. An, Thermophysical Properties of (La0.25Sm0.25Gd0.25Yb0.25)2Ce2+xO7+2x(X=0.1, 0.2, and 0.3) High Entropy Oxides, *Ceram Int*, Elsevier Ltd, 2022, **48**(11), p 14980–14986.

161. H. Zhang, L. Zhao, W. Sang, X. Chen, A. Tang, and H. Zhang, Thermophysical Performances of (La1/6Nd1/6Yb1/6Y1/6Sm1/6Lu1/6)2Ce2O7 High-Entropy Ceramics for Thermal Barrier Coating Applications, *Ceram Int*, Elsevier Ltd, 2022, **48**(2), p 1512–1521.

162. L. Xu, L. Su, H. Wang, H. Gao, D. Lu, K. Peng, M. Niu, and Z. Cai, Tuning Stoichiometry of High-Entropy Oxides for Tailorable Thermal Expansion Coefficients and Low Thermal Conductivity, *Journal of the American Ceramic Society*, John Wiley and Sons Inc, 2022, **105**(2), p 1548–1557.

163. H. Chen, Z. Zhao, H. Xiang, F.Z. Dai, W. Xu, K. Sun, J. Liu, and Y. Zhou, "High Entropy (Y0.2Yb0.2Lu0.2Eu0.2Er0.2)3Al5O12: A Novel High Temperature Stable Thermal Barrier Material," *Journal of Materials Science and Technology*, Chinese Society of Metals, 2020, p 57–62.

164. S. Gu, S. Zhang, F. Liu, Y. Liang, and W. Li, Microstructure and Thermal Shock Performance of Y2Hf2O7 Coating Deposited on SiC Coated C/C Composite, *Appl Surf Sci*, 2018, **455**, p 849–855, doi:https://doi.org/10.1016/j.apsusc.2018.06.073.

165. L. Cong, S. zhang, S. Gu, and W. Li, Thermophysical Properties of a Novel High Entropy Hafnate Ceramic, *J Mat Sci Tech*, Chinese Society of Metals, 2021, **85**, p 152–157.

166. L. Cong, W. Li, J. Wang, S. Gu, and S. zhang, High-Entropy (Y0.2Gd0.2Dy0.2Er0.2Yb0.2)2Hf2O7 Ceramic: A Promising Thermal Barrier Coating Material, *J Mater Sci Technol*, Chinese Society of Metals, 2022, **101**, p 199–204.

167. F. Ye, F. Meng, T. Luo, and H. Qi, The CMAS Corrosion Behavior of High-Entropy (Y0.2Dy0.2Er0.2Tm0.2Yb0.2)4Hf3O12 Hafnate Material Prepared by Ultrafast High-Temperature Sintering (UHS), *J Eur Ceram Soc*, Elsevier Ltd, 2023, **43**(5), p 2185–2195.

168. J. Zhu, X. Meng, J. Xu, P. Zhang, Z. Lou, M.J. Reece, and F. Gao, Ultra-Low Thermal Conductivity and Enhanced Mechanical Properties of High-Entropy Rare Earth Niobates (RE3NbO7, RE = Dy, Y, Ho, Er, Yb), *J Eur Ceram Soc*, Elsevier Ltd, 2021, **41**(1), p 1052–1057.

169. Z. Zhao, H. Chen, H. Xiang, F.Z. Dai, X. Wang, W. Xu, K. Sun, Z. Peng, and Y. Zhou, High Entropy Defective Fluorite Structured Rare-Earth Niobates and Tantalates for Thermal Barrier Applications, *Journal of Advanced Ceramics*, Tsinghua University, 2020, **9**(3), p 303–311.

170. A.J. Wright, Q. Wang, C. Huang, A. Nieto, R. Chen, and J. Luo, From High-Entropy Ceramics to Compositionally-Complex Ceramics: A Case Study of Fluorite Oxides, *J Eur Ceram Soc*, Elsevier Ltd, 2020, **40**(5), p 2120–2129.

Table Captions

Table 1: Properties of HE ceramics introduced as promising TBC topcoat ceramic

Figure Captions

Figure 1: CTE vs. thermal conductivity of different TBC topcoat materials, gathered by Vassen *et al.* (Ref 8)

Figure 2: SEM image of as-sprayed TBC with the L(ZCHST)O topcoat. (a) Full view of cross-section SEM image of as-sprayed TBC, (b) topcoat magnification SEM image, (c)interface between topcoat and bond coat magnification SEM image (Ref 100).

Figure 3: Structural characterization of synthesized ceramics by Song et al., namely (a) XRD patterns, (b) Raman spectrum

Figure 4: Microstructures of $(La_{0.2}Ce_{0.2}Nd_{0.2}Sm_{0.2}Eu_{0.2})_2Zr_2O_7$and $La_2Zr_2O_7$compacts after annealing at 1500◦C for 1–18 h in the air: ((a): 1 h, (b): 6 h, (c): 12 h, (d): 18 h for$(La_{0.2}Ce_{0.2}Nd_{0.2}Sm_{0.2}Eu_{0.2})_2Zr_2O_7$and (e): 1 h, (f): 6 h, (g): 12 h, (h): 18 h for $La_2Zr_2O_7$); published by Zhao et. al (Ref. 99).

Figure 5: Point EDS analysis results of the CMAS corroded specimens after 24 h corrosion, published by Tu *et al.* (Ref 140). Microstructures of (a) $(La_{0.2}Nd_{0.2}Sm_{0.2}Eu_{0.2}Gd_{0.2})_2Zr_2O_7$ (HEZ) and (b) $La_2Zr_2O_7$ (LZ), element contents of (c) residual CMAS.

Figure 6: SEM images of the cross-section of (a) the coating system and (b) the $(La_{0.2}Nd_{0.2}Sm_{0.2}Eu_{0.2}Gd_{0.2})_2Zr_2O_7$ ceramic layer published by Zhou *et al.* (Ref 129).

Figure 7: EDS elemental maps on the polished cross-section of the HE-REZ ceramic coating published by Zhou *et al.* (Ref 129).

Figure 8: XRD pattern of the as-sprayed HE-REZ ceramic coating. The inset is the zoom-in view of (222) peak compared with that of as-synthesized $(La_{0.2}Nd_{0.2}Sm_{0.2}Eu_{0.2}Gd_{0.2})_2Zr_2O_7$ published by Zhou *et al.* (Ref 129).

Figure 9: (a) Photographs of the as-sprayed coating and after the thermal cycling test. (b) XRD pattern of the $(La_{0.2}Nd_{0.2}Sm_{0.2}Eu_{0.2}Gd_{0.2})_2Zr_2O_7$ (HE-REZ) ceramic and LZ coating before and after thermal published by Zhou *et al.* (Ref 129).

Figure 10: SEM images of the cross-sections of the TBCs after the thermal cycling test. (a) $(La_{0.2}Nd_{0.2}Sm_{0.2}Eu_{0.2}Gd_{0.2})_2Zr_2O_7$ (HE-REZ); (b) $La_2Zr_2O_7$ (LZ) published by Zhou *et al.* (Ref 129).

Figure 11: (A-F) The cross-sectional images of CMAS-reacted HE-REZ pellets for 0.5, 1, 2, 4, 12, and 24 h, respectively. (a-f) The corresponding EDS elemental Si maps, published by Deng et al. (Ref 151).

Figure 12: Cross-sectional morphologies (BSE) of 5YH after molten CMAS corrosion at 1300 ℃ for 5 h (a, b and c), 7.5 h (d, e and f) and 10 h (h, i and j) published by Ye et al. (Ref 167).

Figure 13: XRD patterns of the mixed powders of Y_3NbO_7, HE RE_3NbO_7, HE $RE_3(Nb_{1/2}Ta_{1/2})O_7$, and α-$Al_2O_3$ after annealing at different temperatures for 2 h: (a) 1200 ℃, (b) 1250 ℃, and (c) 1300 ℃ published by Zhao et al. (Ref 169).